ARMY RESEARCH LABORATORY

# Navier-Stokes Predictions of the Individual Components of the Pitch-Damping Coefficient Sum

**by Paul Weinacht**

**ARL-TR-3169** **April 2004**

## NOTICES

### Disclaimers

The findings in this report are not to be construed as an official Department of the Army position unless so designated by other authorized documents.

Citation of manufacturer's or trade names does not constitute an official endorsement or approval of the use thereof.

Destroy this report when it is no longer needed. Do not return it to the originator.

**Army Research Laboratory**
Aberdeen Proving Ground, MD 21005-5066

**ARL-TR-3169** **April 2004**

# Navier-Stokes Predictions of the Individual Components of the Pitch-Damping Coefficient Sum

**Paul Weinacht**
**Weapons and Materials Research Directorate, ARL**

# Report Documentation Page

*Form Approved*
*OMB No. 0704-0188*



| 1. REPORT DATE *(DD-MM-YYYY)* | 2. REPORT TYPE | 3. DATES COVERED (From - To) |
|---|---|---|
| April 2004 | Final | 1994–2003 |

**4. TITLE AND SUBTITLE**
Navier-Stokes Predictions of the Individual Components of the Pitch-Damping Coefficient Sum

**5a. CONTRACT NUMBER**

**5b. GRANT NUMBER**

**5c. PROGRAM ELEMENT NUMBER**

**6. AUTHOR(S)**
Paul Weinacht

**5d. PROJECT NUMBER**
1L1612618AH80

**5e. TASK NUMBER**

**5f. WORK UNIT NUMBER**

**7. PERFORMING ORGANIZATION NAME(S) AND ADDRESS(ES)**
U.S. Army Research Laboratory
ATTN: AMSRD-ARL-WM-BC
Aberdeen Proving Ground, MD 21005-5066

**8. PERFORMING ORGANIZATION REPORT NUMBER**
ARL-TR-3169

**9. SPONSORING/MONITORING AGENCY NAME(S) AND ADDRESS(ES)**

**10. SPONSOR/MONITOR'S ACRONYM(S)**

**11. SPONSOR/MONITOR'S REPORT NUMBER(S)**

**12. DISTRIBUTION/AVAILABILITY STATEMENT**
Approved for public release; distribution is unlimited.

**13. SUPPLEMENTARY NOTES**

**14. ABSTRACT**
An approach for predicting the two individual aerodynamic damping coefficients that form the pitch-damping coefficient sum is presented. The coefficients are obtained using prescribed or forced motions that independently excite the two different angular rates that are associated with the two damping coefficients. A key feature of the approach is that steady flow fields are produced by the selected motions. Steady flow computational fluid dynamics approaches can be applied, allowing results to be obtained in a computationally efficient manner. Application of the technique is made to an axisymmetric projectile configuration. The predicted pitch-damping coefficient sum obtained by adding the individually determined coefficients is in excellent agreement with previous predictions of the pitch-damping coefficient sum and with experimental data. Additional validation of the approach is obtained through comparisons with prior results from numerical solutions of the nonlinear unsteady potential equation. The individual coefficients are also compared with slender body theory, and the results show similar trends though the slender body theory appears to underpredict the various coefficients.

**15. SUBJECT TERMS**
aerodynamics, projectile flight mechanics, pitch-damping

| 16. SECURITY CLASSIFICATION OF: | | | 17. LIMITATION OF ABSTRACT | 18. NUMBER OF PAGES | 19a. NAME OF RESPONSIBLE PERSON |
|---|---|---|---|---|---|
| a. REPORT | b. ABSTRACT | c. THIS PAGE | | | Paul Weinacht |
| UNCLASSIFIED | UNCLASSIFIED | UNCLASSIFIED | UL | 44 | 19b. TELEPHONE NUMBER (*Include area code*) 410-278-4280 |

**Standard Form 298 (Rev. 8/98)**
Prescribed by ANSI Std. Z39.18

## Contents

## List of Figures

## List of Tables

INTENTIONALLY LEFT BLANK.

# 1. Introduction

Traditionally in aeroballistic applications, the pitch-damping coefficient has been treated as the sum of two individual coefficients that produce an aerodynamic moment proportional to the angular rate associated with the angle of attack. In fact, these two individual coefficients represent moments proportional to two different angular rates, although for many nonmaneuvering flight trajectories, including those flown in ballistic aerodynamic ranges, these two angular rates are essentially equivalent. For this reason, the pitch-damping coefficient sum is often treated as a single parameter. In some cases, such as for maneuvering flight vehicles, the simplification that the two angular rates are equivalent is no longer valid, and the two individual components of the pitch-damping coefficient sum must be determined independently. Experimental determination of these coefficients is difficult at best and is probably not possible using traditional aerodynamic ranges.

Prior research has focused on the development and application of computational methods for predicting the pitch-damping coefficient sum. The basis of the technique is to impose a particular motion (coning motion) on the flight vehicle, which produces moments that are proportional to the pitch-damping coefficient sum. Because coning motion produces a steady flow field in the cases of interest, efficient numerical techniques can be readily applied and the pitch-damping coefficient sum determined in a cost-efficient manner. These techniques have been benchmarked with experimental data, and good agreement between computation and experiment has been found for a number of flight vehicle geometries (*1–10*).

In the current effort, the method is extended so that the individual components of the pitch-damping coefficient can be determined independently. The method uses imposed motions that excite the two angular rates independently so that the forces and moments attributable to these rates can be assessed separately. A key feature of the approach is that the motions produce steady flow fields that can be computed in a cost-efficient manner. The techniques described here represent a unique aerodynamic capability for a problem that is difficult to address experimentally. Other than approximate methods, these results most likely represent the first numerical predictions of the individual components of the pitch-damping coefficient sum for flight vehicles. Subsequent to its original publication (*8–10*), the technique has also been adopted by other researchers (*11*).

This report presents a derivation of the transverse aerodynamic force and moment equations associated with the motions of interest using a general force and moment expansion for symmetric flight bodies. The resulting equations demonstrate that the aerodynamic forces and moments can be excited independently using the appropriate motions. Results are presented for a family of axisymmetric flight bodies at supersonic flight velocities. A schematic of the Army-Navy spinner rocket (ANSR) flight body geometries is shown in figure 1. Both of the

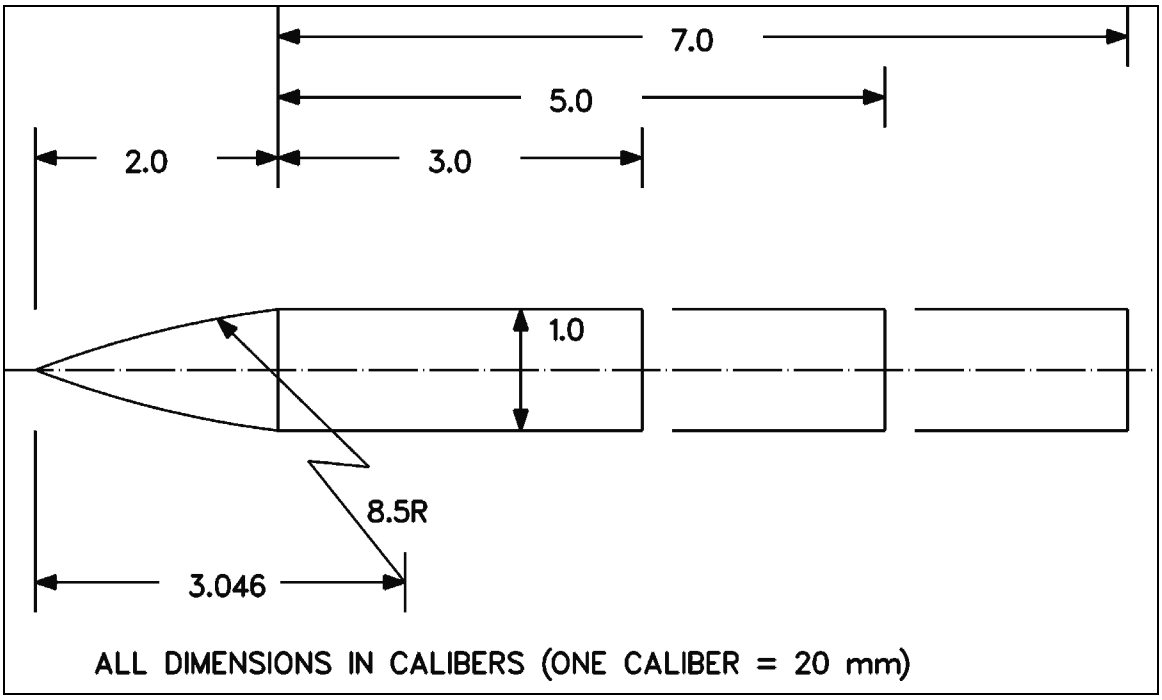


Figure 1. Schematic of ANSR configuration.

components ( $C_{m_q}$ and $C_{m_{\dot{\alpha}}}$ ) of the pitch-damping coefficient sum, $C_{m_q} + C_{m_{\dot{\alpha}}}$ , are determined independently. Comparison of the predicted aerodynamic coefficients is made with slender body theory and numerical solutions of the nonlinear unsteady potential equation. The sum of the two individually determined coefficients is also compared with the pitch-damping coefficient sum, $C_{m_q} + C_{m_{\dot{\alpha}}}$ , determined from coning motion. Both methods of determining the pitch-damping coefficient sum are in good agreement with experimental data.

## 2. Theoretical Background

### 2.1 The Force and Moment Expansion

It is common in many aerodynamics applications to use a body-fixed, nonrolling coordinate system to describe both the dynamics and the system of forces and moments that act on the flight vehicle (*12*). The nonrolling coordinate system allows the description of the vehicle dynamics to be simplified for certain classes of flight vehicles that possess particular types of geometric symmetry. Rotationally symmetric flight vehicles, which are the focus of the current research, represent one class of vehicles where the nonrolling frame has been effectively (and traditionally) used. For more complicated geometries, such as aircraft, the advantages of the nonrolling frame are reduced and other coordinate frames such as a completely body-fixed coordinate system are typically used.

In the current effort, the primary reason for initially describing the aerodynamic forces and moments using the nonrolling coordinate system is the fact that the description is well established for symmetric flight vehicles. The nonrolling coordinate frame is an orthogonal right-handed system $(\tilde{x}, \tilde{y}, \tilde{z})$ centered at the body's center of gravity (CG). The $\tilde{x}$-axis is aligned along the projectile longitudinal axis with the positive direction oriented toward the projectile nose. The $\tilde{z}$-axis is "initially" oriented downward with the $\tilde{x}$-$\tilde{z}$ plane perpendicular to the ground. The angular motion of the nonrolling coordinate frame is such that, with respect to an inertial frame, the $\tilde{x}$-component of the coordinate frame's angular velocity is zero. Although the time-dependent orientation of the nonrolling frame may be difficult to visualize, the nonrolling frame is essentially equivalent to the "fixed-plane" coordinate system for small amplitude motions. In the fixed-plane coordinate system, the $\tilde{x}$-$\tilde{z}$ plane remains perpendicular to the ground for all time. The total angular velocity of the flight vehicle can be described in terms of its angular velocity components $(p, \tilde{q}, \tilde{r})$ along the $\tilde{x}$, $\tilde{y}$, and $\tilde{z}$ axes, respectively. The angular velocity of the nonrolling frame can be described in terms of the transverse angular velocities $\tilde{q}$ and $\tilde{r}$ because the angular velocity of the nonrolling frame along the $\tilde{x}$-axis is always zero. The flight body may, however, have a nonzero spin rate, p, about its longitudinal axis. Further details about these coordinate frames are discussed in reference (*12*).

The moment expansion for a rotationally symmetric missile in the nonrolling coordinate frame is shown in equation 1. This moment expansion is similar to the moment proposed by Murphy (*12*). The moment formulation uses complex variables to separate the moment components, $\tilde{C}_m$ and $\tilde{C}_n$, that are oriented along the $\tilde{y}$ and $\tilde{z}$ axes, respectively. The third moment component, the roll moment, can be handled separately and is not of consequence in this study.

$$\tilde{C}_m + i\tilde{C}_n = \left[\left(\frac{p\ell}{V}\right)C_{n_{p\alpha}} - iC_{m_\alpha}\right]\tilde{\xi} + C_{m_q}\tilde{\mu} - iC_{m_{\dot{\alpha}}}\tilde{\xi}'. \tag{1}$$

In the moment expansion, the pitching moment coefficient slope, $C_{m_\alpha}$, and the coefficient $C_{m_{\dot{\alpha}}}$ represent moments that are proportional to the complex yaw, $\tilde{\xi}$, and yawing rate, $\tilde{\xi}'$, respectively.

The complex yaw and yawing rate are defined as follows. (In the analysis presented here, there is no need to distinguish between pitch and yaw, and the terms may be interchanged.) The usage follows that of Murphy (*12*).

$$\tilde{\xi} = \frac{\tilde{v} + i\tilde{w}}{V}, \tag{2}$$

and

$$\tilde{\xi}' = \frac{d\tilde{\xi}}{d\left(\frac{s}{\ell}\right)}. \tag{3}$$

Here, $\tilde{v}$ and $\tilde{w}$ are the $\tilde{y}$- and $\tilde{z}$-components of the velocity vector, $\vec{V}_\infty$, that describes the velocity of the body CG relative to the inertial frame. The magnitude of this vector is denoted as V. The angular rate is obtained by taking the derivative of the complex yaw with respect to the flight path coordinate, s, which is nondimensionalized by some characteristic length, $\ell$, typically the body diameter.

The coefficient, $C_{m_q}$, represents a moment that is proportional to the complex transverse angular velocity of the vehicle, $\tilde{\mu}$, as defined in the following:

$$\tilde{\mu} = \frac{(\tilde{q} + i\tilde{r})\ell}{V}. \tag{4}$$

Here, $\tilde{q}$ and $\tilde{r}$ are the $\tilde{y}$- and $\tilde{z}$-components of angular velocity of the vehicle in the nonrolling coordinate system. The remaining coefficient in the moment expansion, the Magnus moment coefficient, $C_{n_{p\alpha}}$, accounts for a side moment due to flow asymmetries produced by the combination of spin and yaw.

It should be noted that the moment formulation neglects the variation of the moments with roll angle under the assumption that these variations are small. For axisymmetric vehicles, the variations with roll angle should not exist because the geometry will not change as the roll orientation changes. Roll variations in the aerodynamic coefficients for other types of rotationally symmetric vehicles are typically negligible for small amplitude motions. In general, roll variations may be difficult to detect in flight because the effect of roll orientation tends to be averaged out over the course of a yaw cycle if the body is spinning.

### 2.2 Planar Motions

For planar motions, the aerodynamic moments that act on an axisymmetric flight body can be written in terms of the following expansion. The force expansion has a similar form.

$$\tilde{C}_m + i\tilde{C}_n = \left[ i\left(\frac{p\ell}{V}\right)C_{n_{p\alpha}} + C_{m_\alpha} \right]\sin\alpha + C_{m_q}\left(\frac{q\ell}{V}\right) + \gamma\, C_{m_{\dot\alpha}}\left(\frac{\dot\alpha\ell}{V}\right). \tag{5}$$

Two damping moments, $C_{m_{\dot\alpha}}$ and $C_{m_q}$, represent moments proportional to the angular rates $\dot\alpha$ and q that are associated with the angle of attack, $\alpha$, and the angular displacement of the longitudinal axis of the body with respect to the earth-fixed axis system denoted by the angle, $\theta$, respectively. These angles are displayed schematically in figure 2 for the case of planar motion.

For a typical ballistic trajectory, over the course of many yaw cycles, the flight body will travel a nearly rectilinear flight path. In this case, the free-stream velocity vector, $\vec{V}_\infty$, has a fixed orientation with respect to the earth-fixed axes, $x_e$ and $z_e$. For a rectilinear flight path, the angular rates $\dot\alpha$ and q will be equal. The moment expansion can be simplified by combining the two damping coefficients into a single coefficient sum, which is proportional to a single angular

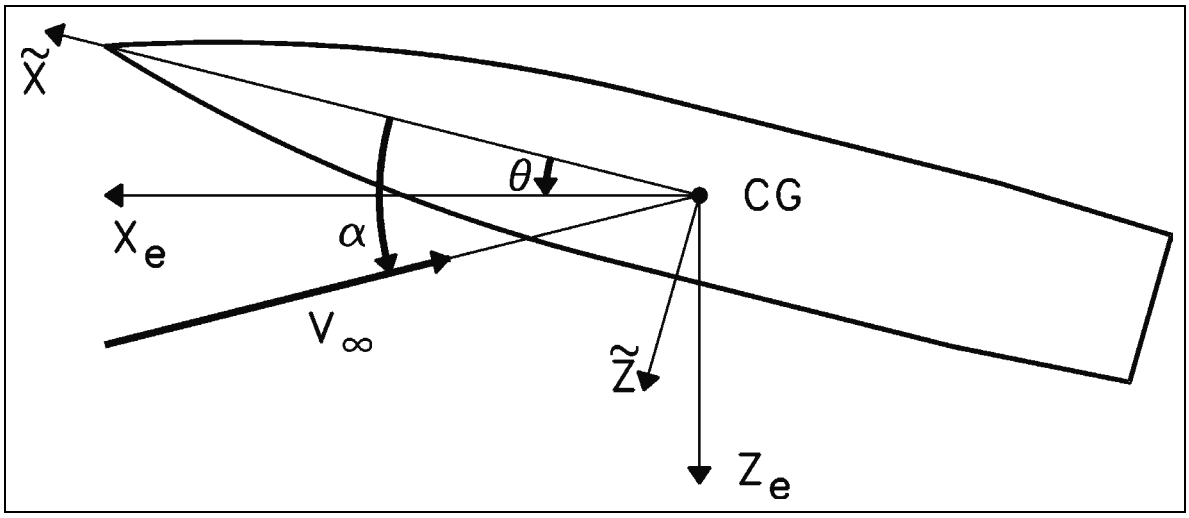


Figure 2. Angular orientation of projectile relative to velocity vector and earth-fixed coordinate frame.

rate (either $\dot{\alpha}$ or q). For maneuvering flight bodies, this simplification may not be valid, and the individual coefficients must be treated independently.

To produce aerodynamic moments proportional to the damping terms, one or both of the angular velocities must be nonzero. One simple planar motion that produces a nonzero q and zero $\dot{\alpha}$ angular velocity is a circular looping motion as shown in figure 3. If such a motion is performed at constant angular velocity, $\Omega$, $(q = \dot{\theta} = \Omega)$, and constant angle of attack (which may or may not be zero), the following form of the force and moment expansions results:

$$\tilde{C}_m + i\tilde{C}_n = \left[ i\left(\frac{p\ell}{V}\right) C_{n_{p\alpha}} + C_{m_\alpha} \right] \sin\alpha + C_{m_q}\left(\frac{\Omega\ell}{V}\right). \tag{6}$$

Here, the in-plane moment, $C_m$, contains contributions from both the pitching moment slope, $C_{m_\alpha}$, and the pitch-damping coefficient, $C_{m_q}$. The side moment, $C_n$, is identical in form to the side moment due to constant $\alpha$ motion and is independent of the angular rate q. Because the damping terms are independent of the spin rate and the side moment is independent of the angular rate q, the spin rate is assumed to be zero to simplify the discussion of the looping motion that follows.

With respect to the inertial frame of reference, the flow field is periodic and unsteady. However, in the nonrolling frame (shown in figure 3 as the $\tilde{x} - \tilde{z}$ axes), the flow field is potentially steady. Indeed, the moment expansion displays no unsteadiness since all the terms on the right-hand side are constants. Because the flow field is potentially steady in the nonrolling frame for this type of motion, this frame is suitable for use with computational approaches that are based on steady flow techniques.

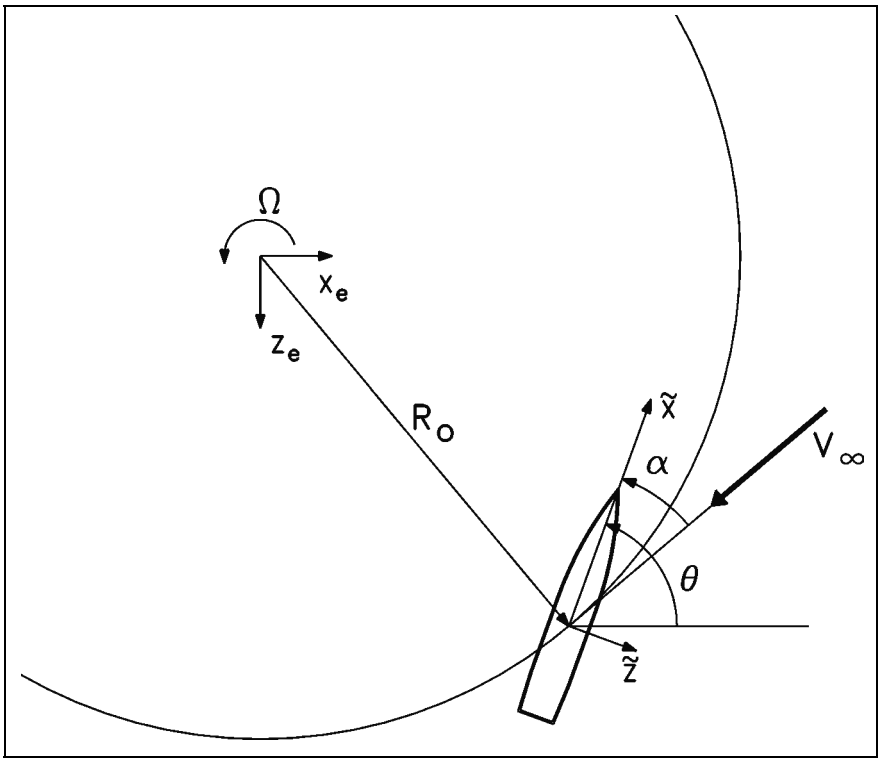


Figure 3. Schematic of planar looping motion.

For looping motion, the moment expansion contains contributions from two of the aerodynamic coefficients. The contribution from the pitching moment coefficient slope, $C_{m_\alpha}$, can be eliminated if the body longitudinal axis is tangent to the radius of curvature of the loop. In this case, the angle of attack is zero, and the damping moment, $C_{m_q}$, is directly proportional to the net aerodynamic moment. If the damping moment exhibits a dependence on angle of attack, several experiments or computations involving different looping rates must be performed for each angle of attack. (If the looping rate is varied, the loop radius must also be changed to maintain a constant vehicle velocity: $V = \Omega R_o$.) The damping moment can be obtained by computing the variation in the net aerodynamic moment with looping rate. If the net aerodynamic moment displays a nonlinear variation with both angle of attack and looping rate, it may be difficult to separate the contributions attributable to the $C_{m_\alpha}$ and $C_{m_q}$, without additional information or assumptions. In general, variations of the coefficients with angle of attack might be reasonably expected, while variations in the coefficients with angular rate are less common. In any event, the looping motion can be used to check for these types of nonlinear variations.

One feature of this type of motion is that high angular velocities or large loop radii are required to generate high velocities, making this type of motion impractical for use in experimental testing. However, this is not a problem for computational approaches because large loop radii or high angular velocities can be easily accommodated.

## 2.3 Helical Motions

Other more complicated motions can be proposed, which produce aerodynamic moments proportional to the angular rates, $\tilde{\mu}$ and $\tilde{\xi}'$, while still producing steady flow fields when viewed from the appropriate coordinate frame. Two such motions require the CG of the flight vehicle to traverse a helical flight path. The first motion requires the vehicle's longitudinal axis to be oriented in the same direction as the center of rotation of the helix but displaced by a constant distance. Figure 4 shows a three-dimensional (3-D) view of the motion. A two-dimensional (2-D) projection of this motion on the vertical plane is shown in figure 5. This particular motion produces no rotation of the nonrolling coordinate frame relative to an earth-fixed coordinate frame, and hence, the angular velocity $\tilde{\mu}$ is zero. The angle of attack and its angular rate vary continuously, producing moment components associated with the coefficients $C_{m_\alpha}$ and $C_{m_{\dot{\alpha}}}$, respectively. This motion is referred to as "q = 0 helical motion" because the angular rates associated with the damping coefficient $C_{m_q}$ are zero.

For the second motion, the longitudinal axis of the flight vehicle remains tangent to the helical flight path at each point along the trajectory. Figure 6 shows a 3-D view of this motion. A 2-D projection of this motion on the vertical plane is also shown in figure 7. The angle of attack of the incident airstream is zero because both the longitudinal axis of the body and the free-stream velocity vector are tangent to the flight path. The resulting yawing rate is also zero because the angle of attack is constant. The angular orientation of the flight body changes continuously with respect to an earth-fixed reference frame, producing a nonzero angular rate, $\tilde{\mu}$. As a result, moment components associated with the damping moment $C_{m_q}$ are produced. This motion is referred to as "$\dot{\alpha} = 0$ helical motion" because the angular rates associated with the damping coefficient $C_{m_{\dot{\alpha}}}$ are zero. The $\dot{\alpha} = 0$ helical motion produces a steady flow field when viewed from the appropriate coordinate system, while its 2-D projection is clearly time dependent.

The net transverse aerodynamic moment in the nonrolling frame can be determined for each of the motions by substituting the appropriately determined angle of attack, $\tilde{\xi}$, and angular rates, $\tilde{\xi}'$ and $\tilde{\mu}$, into equation 1. The angle of attack and angular rates for both types of helical motion are shown in equations 7–14.

**q = 0 Helical Motion**

$$\tilde{\xi} \equiv \frac{\tilde{v} + i\tilde{w}}{V} = -\delta\, e^{i\Omega t}, \tag{7}$$

$$\delta = \frac{R_o \Omega}{\sqrt{U^2 + \Omega^2 R_o^2}} = \frac{R_o \Omega}{V}, \tag{8}$$

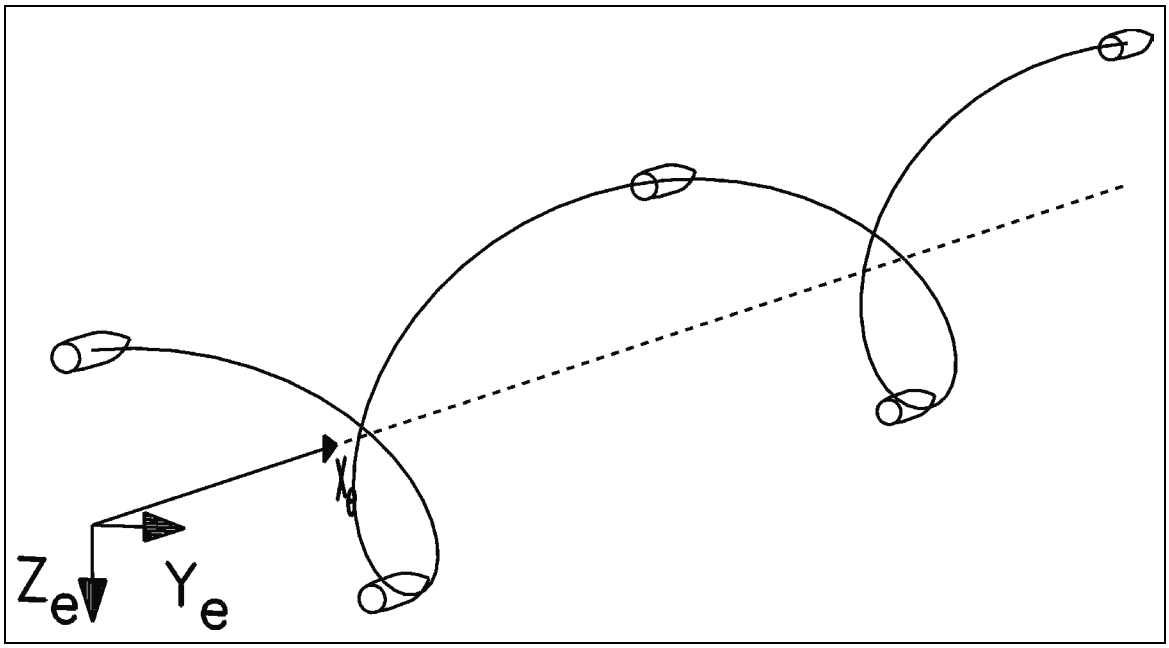


Figure 4. Helical motion with nonzero $\tilde{\dot{\alpha}}$ and zero $\tilde{\mathrm{q}}$.

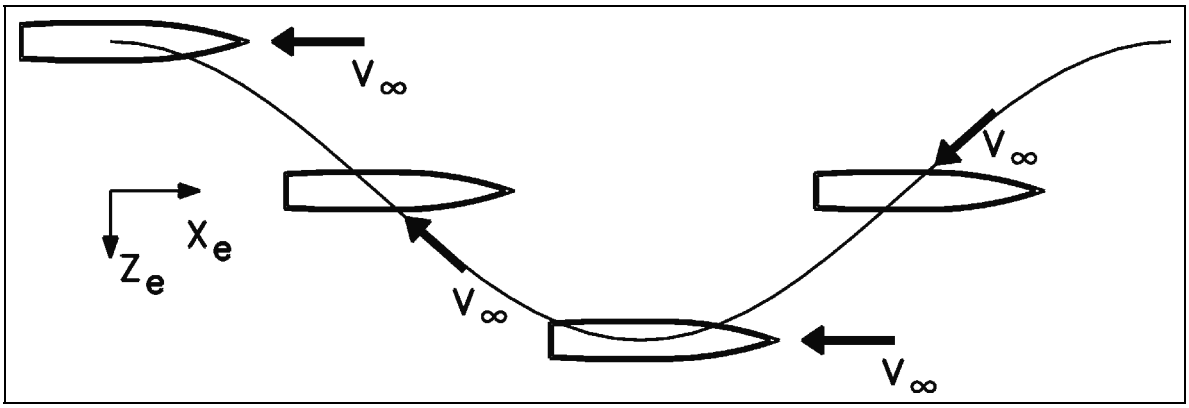


Figure 5. Vertical projection of helical motion with nonzero $\tilde{\dot{\alpha}}$ and zero $\tilde{\mathrm{q}}$.

$$\tilde{\xi}' = -\mathrm{i}\left(\frac{\Omega\ell}{\mathrm{V}}\right)\delta\, \mathrm{e}^{\mathrm{i}\Omega t}, \tag{9}$$

and

$$\tilde{\mu} = 0\,. \tag{10}$$

**$\dot{\alpha} = 0$ Helical Motion**

$$\tilde{\mu} \equiv \frac{\left(\tilde{\mathrm{q}} + \mathrm{i}\tilde{\mathrm{r}}\right)\ell}{\mathrm{V}} = \frac{\Omega\ell}{\mathrm{V}}\left(\sin\beta\right)\mathrm{e}^{\mathrm{i}\Omega t\cos\beta}, \tag{11}$$

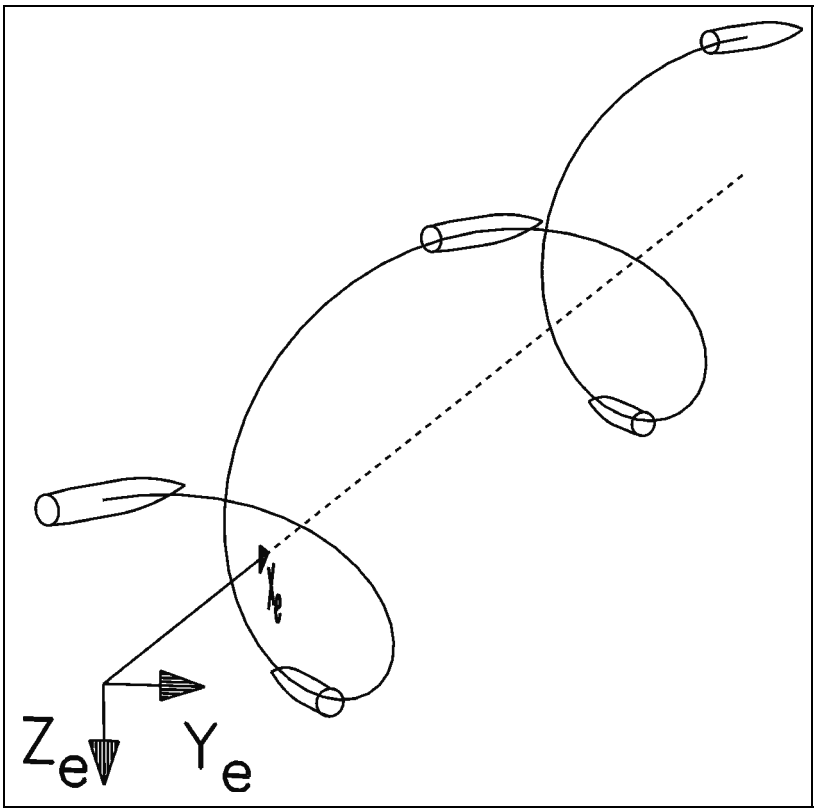


Figure 6. Helical motion with zero $\tilde{\alpha}$ and nonzero $\tilde{q}$ .

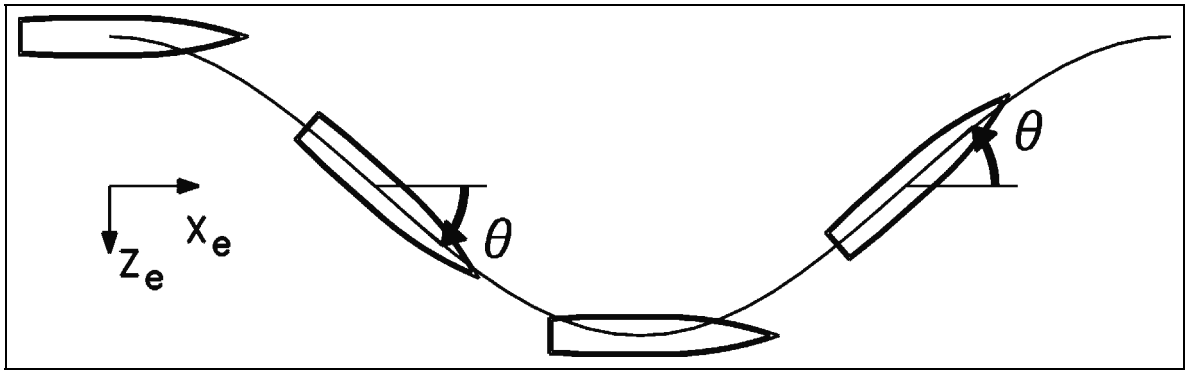


Figure 7. Vertical projection of helical motion with zero $\tilde{\alpha}$ and nonzero $\tilde{q}$ .

$$\cos\beta = \frac{U}{V}, \tag{12}$$

$$\sin\beta = \frac{R_o\Omega}{V}, \tag{13}$$

and

$$\tilde{\xi} = \tilde{\xi}' = 0\,. \tag{14}$$

Here, $\Omega$ is the angular velocity of the body about the helix axis, $R_o$ is the perpendicular distance between the helix axis and the body CG, U is the component of velocity along the helix axis, and V is the total linear velocity of the CG.

To completely define the motions, the spin rate of the body p needs to be specified. It is convenient to set the spin rate of the body p to zero because this will eliminate the contribution to the net aerodynamic moment from the Magnus moment, although this is not required for the $\dot{\alpha} = 0$ helical motion because the complex angle of attack is also zero. Zero spin rate is obtained by the addition of a second angular velocity oriented along the flight body's longitudinal axis that is equal and opposite of the longitudinal component of the angular velocity required to produce the rotation about the axis of the helix. This second angular velocity has no effect on the transverse angular velocities $\tilde{q}$ and $\tilde{r}$.

For each of the helical motions, the transverse aerodynamic moment in the nonrolling frame will be periodic in time, which also indicates that the flow field will be periodic in time when viewed from the nonrolling coordinate frame. However, for both types of helical motion, a steady flow field should be observed when examined from an orthogonal right-handed coordinate system that has its x-axis aligned with the longitudinal axis of the body and its z-axis along a line between the body CG and the axis of rotation of the helix. The transverse aerodynamic moments in the nonrolling frame can be transformed to the coordinate frame where the steady flow field exists, using the following relations:

**q = Helical Motion**

$$C_m + iC_n = \left(\tilde{C}_m + i\tilde{C}_n\right)e^{-i\Omega t}\,, \tag{15}$$

**$\dot{\alpha} = 0$ Helical Motion**

$$C_m + iC_n = \left(\tilde{C}_m + i\tilde{C}_n\right)e^{-i\Omega t\cos\beta}\,. \tag{16}$$

Here, the transverse moments, $C_m$ and $C_n$, refer to the moments about the y- and z-axes, respectively.

Using this transformation, the transverse moments can be shown to have the following form for each of the two types of helical motion.

**q = Helical Motion**

$$C_m + iC_n = -C_{m_{\dot{\alpha}}}\left(\frac{\Omega\ell}{V}\right)\frac{R_o\Omega}{V} + iC_{m_\alpha}\frac{R_o\Omega}{V}\,, \tag{17}$$

**$\dot{\alpha} = 0$ Helical Motion**

$$C_m + iC_n = C_{m_q}\left(\frac{\Omega \ell}{V}\right)\frac{R_o \Omega}{V}. \tag{18}$$

The resulting expressions for the transverse moments are independent of time, indicating that the flow field is potentially steady as well.

Similar expressions for the individual damping force coefficients can be developed using the same approach as applied for the moment coefficients.

**q = Helical Motion**

$$C_Y + iC_Z = iC_{N_{\dot{\alpha}}}\left(\frac{\Omega \ell}{V}\right)\frac{R_o \Omega}{V} + iC_{N_\alpha}\frac{R_o \Omega}{V}, \tag{19}$$

**$\dot{\alpha} = 0$ Helical Motion**

$$C_Y + iC_Z = -iC_{N_q}\left(\frac{\Omega \ell}{V}\right)\frac{R_o \Omega}{V}. \tag{20}$$

### 2.4 CG Translation Relations

If the aerodynamic coefficients have been established for a baseline configuration, it is possible to determine the aerodynamic coefficients for the identical configuration which has a different axial CG location using the CG translation relations (*12*). The CG translation relations for the damping coefficients are shown in equations 21–24. In the context of the current study, the CG translation relations can be used to further validate the results by comparing the theoretical variation of the damping coefficients with CG location with the CFD predictions.

$$\hat{C}_{N_{\dot{\alpha}}} = C_{N_{\dot{\alpha}}}, \tag{21}$$

$$\hat{C}_{N_q} = C_{N_q} + s_{cg} C_{N_\alpha}, \tag{22}$$

$$\hat{C}_{m_{\dot{\alpha}}} = C_{m_{\dot{\alpha}}} + s_{cg} C_{N_{\dot{\alpha}}}, \tag{23}$$

and

$$\hat{C}_{m_q} = C_{m_q} - s_{cg}(C_{N_q} - C_{m_\alpha}) - s_{cg}^2 C_{N_\alpha}. \tag{24}$$

## 3. Computational Approach

Computation of the viscous flow field about the flight body was accomplished by solving the thin-layer Navier-Stokes equations using a parabolized Navier-Stokes (PNS) technique. Because

the computations are performed in a noninertial rotating coordinate frame, the governing equations have been modified to include the body force terms that result from the Coriolis and centripedal accelerations in the rotating coordinate frame. The fluid flow relative to the rotating coordinate frame does not vary with time, allowing the steady (nontime varying) Navier-Stokes equations to be applied. The solution of the steady Navier-Stokes equations can be performed at a reasonable computational cost. The steady thin-layer Navier-Stokes equations are shown as follows:

$$\frac{\partial \hat{E}}{\partial \xi}+\frac{\partial \hat{F}}{\partial \eta}+\frac{\partial \hat{G}}{\partial \zeta}+\hat{H}_c+\hat{H}=\frac{1}{Re}\left(\frac{\partial \hat{S}}{\partial \zeta}+\hat{S}_c\right). \tag{25}$$

Here, $\hat{E}$, $\hat{F}$, and $\hat{G}$ are the inviscid flux vectors, $\hat{S}$ is the viscous flux vector, $\hat{H}_c$ and $\hat{S}_c$ are inviscid and viscous source terms due to the cylindrical coordinate formulation, and $\hat{H}$ is the source term containing the Coriolis and centrifugal force terms that result from the rotating coordinate frame. Each of these matrices is a function of the dependent variables represented by the vector $q^T=(\rho,\rho u,\rho v,\rho w,e)$, where $\rho$ and e are the density and the total energy per unit volume, and u, v, and w, are the velocity components in axial, circumferential, and normal directions. The flux terms are shown as follows:

$$\hat{E}=\frac{1}{J}\begin{bmatrix}\rho U\\ \rho uU+\xi_x p\\ \rho vU\\ \rho wU\\ (e+p)U\end{bmatrix} \qquad \hat{F}=\frac{1}{J}\begin{bmatrix}\rho V\\ \rho uV+\eta_x p\\ \rho vV+\eta_\phi p/r\\ \rho wV+\eta_r p\\ (e+p)V\end{bmatrix}$$

$$\hat{G}=\frac{1}{J}\begin{bmatrix}\rho W\\ \rho uW+\zeta_x p\\ \rho vW+\zeta_\phi p/r\\ \rho wW+\zeta_r p\\ (e+p)W\end{bmatrix} \qquad \hat{H}=\frac{1}{J}\begin{bmatrix}0\\ \rho f_x\\ \rho f_\phi\\ \rho f_r\\ \rho u f_x+\rho v f_\phi+\rho w f_r\end{bmatrix}, \tag{26}$$

where

$$\begin{aligned}U&=u\xi_x\\ V&=u\eta_x+v\eta_\phi/r+w\eta_r\\ W&=u\zeta_x+v\zeta_\phi/r+w\zeta_r,\end{aligned} \tag{27}$$

and

$$\xi_x = 1/x_\xi \qquad \eta_x = J\left(r_\xi \phi_\zeta - \phi_\xi r_\zeta\right)$$
$$\eta_\phi = J(x_\xi r_\zeta) \qquad \eta_r = J\left(-x_\xi \phi_\zeta\right)$$
$$\zeta_x = J\left(\phi_\xi r_\eta - r_\xi \phi_\eta\right) \qquad \zeta_\phi = J(-x_\xi r_\eta)$$
$$\zeta_r = J(x_\zeta \phi_\eta)$$

$$J = 1/[x_\xi(\phi_\eta r_\zeta - \phi_\zeta r_\eta)]. \tag{28}$$

The Coriolis and centrifugal acceleration terms, due to the rotating coordinate system, which are contained in the source term, $\hat{H}$, are shown as follows:

$$\vec{f} = 2\vec{\Omega} \times \vec{u} + \vec{\Omega} \times \left(\vec{\Omega} \times \vec{R}\right). \tag{29}$$

The Coriolis acceleration is a function of the angular velocity of the coordinate frame with respect to the inertial frame, $\vec{\Omega}$, and the fluid velocity vector, $\vec{u}$, which can be represented by the velocity components, u, v, and w. The centripedal acceleration is a function of the angular velocity of the rotating frame, $\vec{\Omega}$, and the displacement vector, $\vec{R}$, between the axis of rotation and the local position in the flow field. The acceleration vector, $\vec{f}$, can be written in terms of its components along the x, $\phi$ and r axes, $f_x$, $f_\phi$, and $f_r$.

The angular velocities for the three different motions considered in this study are written in the following. The angular velocities are nondimensionalized in a manner consistent with the Navier-Stokes equations.

**Looping Motion**

$$\vec{\Omega} = \left(\frac{\Omega D}{a_\infty}\right)\cos\phi\,\vec{i}_\phi - \left(\frac{\Omega D}{a_\infty}\right)\sin\phi\,\vec{i}_r, \tag{30}$$

**$\dot{\alpha} = 0$ Helical Motion**

$$\vec{\Omega} = \left(\frac{\Omega D}{a_\infty}\right)\vec{i}_x, \tag{31}$$

**q = Helical Motion**

$$\vec{\Omega} = \left(\frac{\Omega D}{a_\infty}\right)\cos\beta\,\vec{i}_x + \left(\frac{\Omega D}{a_\infty}\right)\sin\beta\cos\phi\,\vec{i}_\phi - \left(\frac{\Omega D}{a_\infty}\right)\sin\beta\sin\phi\,\vec{i}_r. \tag{32}$$

The pressure, p, can be related to the dependent variables by applying the ideal gas law:

$$p = (\gamma - 1)\left[e - \frac{\rho}{2}\left(u^2 + v^2 + w^2\right)\right]. \tag{33}$$

The turbulent viscosity, $\mu_t$, which appears in the viscous matrices, was computed using the Baldwin-Lomax turbulence model (*13*).

The thin-layer equations are solved using the PNS technique of Schiff and Steger (*14*). Following the approach of Schiff and Steger, the governing equations, which have been modified here to include the Coriolis and centrifugal force terms, are solved using a conservative, approximately factored, implicit finite-difference numerical algorithm as formulated by Beam and Warming (*15*). Details of the implementation of the source term that contains the Coriolis and centrifugal force terms are given in reference (*5*).

The computations presented here were performed using a shock-fitting procedure (*16*). This procedure solves the five Rankine-Hugoniot jump conditions, two geometric shock propagation conditions, and one compatibility equation to determine the values of the five dependent variables immediately behind the shock, as well as the position of the shock. By including the implicit part of the source term due to the rotating coordinate frame in the circumferential inversion, the shock-fitting procedure can be used without modification, as long as the free-stream conditions are modified to account for the rotating coordinate frame.

At the body surface, no-slip, constant wall temperature boundary conditions were applied. For the helical motions, the tangential velocity at the body surface was set equal to the local velocity of the body surface due to the solid-body rotation produced by an angular velocity equal and opposite to the longitudinal component of angular velocity shown in equations 31 and 32. This is required to produce a zero spin rate p in the nonrolling coordinate frame.

An initial solution for the PNS marching procedure was obtained using a conical step-back procedure at a location of 0.2 body diameters from the nosetip. Although the perturbations to the flow field from the helical motions are not compatible with the conical flow assumption, the effect on the solution appears to be small. Moving the starting plane to 0.1 body diameters from the nose tip resulted in <0.5% variation in the computed damping moments.

The computational results presented here were obtained using a grid that consisted of 60 points between the body and the shock. In the circumferential direction, gridding was performed over a 360° sector because of the lack of symmetry from the combination of angle of attack, spin, and coning or helical motion. Thirty-six grid points were used in the circumferential direction. In longitudinal direction, 78 marching steps were utilized for each body diameter of length. To ensure adequate grid resolution within the boundary layer, the grid spacing at the body surface was adapted to maintain nondimensional boundary layer coordinate $y^+$ between 2 and 3 in accordance with previously published results (*17*). Grid resolution studies for the 9-caliber body (middle CG location) showed <2% variation in the computed pitch-damping coefficient sum when the grid resolution was decreased by 25% in each of the three coordinate directions. Similarly, when the grid in the circumferential and marching directions was doubled and the grid in the radial direction was increased by 50%, the computed pitch-damping coefficient sum varied

by only 1%. Differences in the damping coefficient $C_{m_q}$ on the coarse and fine mesh, relative to the baseline grid, were <1%. The damping coefficient $C_{m_{\dot{\alpha}}}$ showed a larger variability on a percentage basis on the coarse and fine grid relative to the baseline grid (6% and 3%, respectively), although absolute differences between the predicted values of the coefficient were similar to the differences between the predicted pitch-damping coefficient sum. The smaller magnitude of $C_{m_{\dot{\alpha}}}$, relative to the pitch-damping coefficient sum, contributed to a larger percentage error. The computations for the baseline grid, which were performed using a Cray Y-MP supercomputer, typically required <10 min of CPU time for complete calculation over a single configuration.

## 4. Results

Computations of the individual coefficients that comprise the pitch-damping force and moment coefficient sums were performed using helical and looping motions. The computations were performed for the ANSR series of bodies shown in figure 1. Results for length-to-diameter (L/D) ratio = 5, 7, and 9 bodies are presented here for flight velocities of Mach 1.8 and 2.5. Three different CG locations were considered for each body length, as shown in table 1. Aerodynamic range tests of the ANSR (*18*) were used to benchmark the predicted pitch-damping coefficient sum.

Table 1. CG location for ANSR flight bodies.

| | **Longitudinal CG (Calibers From Nose)** | | |
|---|---|---|---|
| **L/D** | **Forward** | **Middle** | **Rearward** |
| 5 | 2.5 | 3.0 | 3.5 |
| 7 | 3.251 | 4.037 | 4.812 |
| 9 | 4.0 | 5.038 | 5.885 |

The effect of angular rate and the rotational velocity ratio for the q = 0 helical motion and $\dot{\alpha} = 0$ helical motion was examined for the L/D = 9 ANSR body (forward CG) at a flight velocity of Mach 2.5. The force and moment expansion for both of these motions indicates a linear variation of the forces and moments is expected with angular rate and rotational velocity ratio within the regime where linear aerodynamic theory is expected to be valid. The predictions were performed for the longest ANSR body because the longer bodies typically exhibit more nonlinear aerodynamic behavior. Thus, the onset of nonlinear behavior of the aerodynamics with angular rate or angle of attack would be more evident, and the limits of linear aerodynamic behavior could be more readily identified.

The effect of angular rate for the q = 0 motion was examined by performing computations at several angular velocities but at a fixed total angle of attack of 2°. This means that as the angular velocity was increased, the radius $R_o$ was decreased so that the product $R_o\Omega$ (and the total angle of attack) was constant. Figure 8 shows the variation of the aerodynamic moment $C_m$ with angular velocity, and the variation is seen to be linear across the range of angular velocities of interest here.

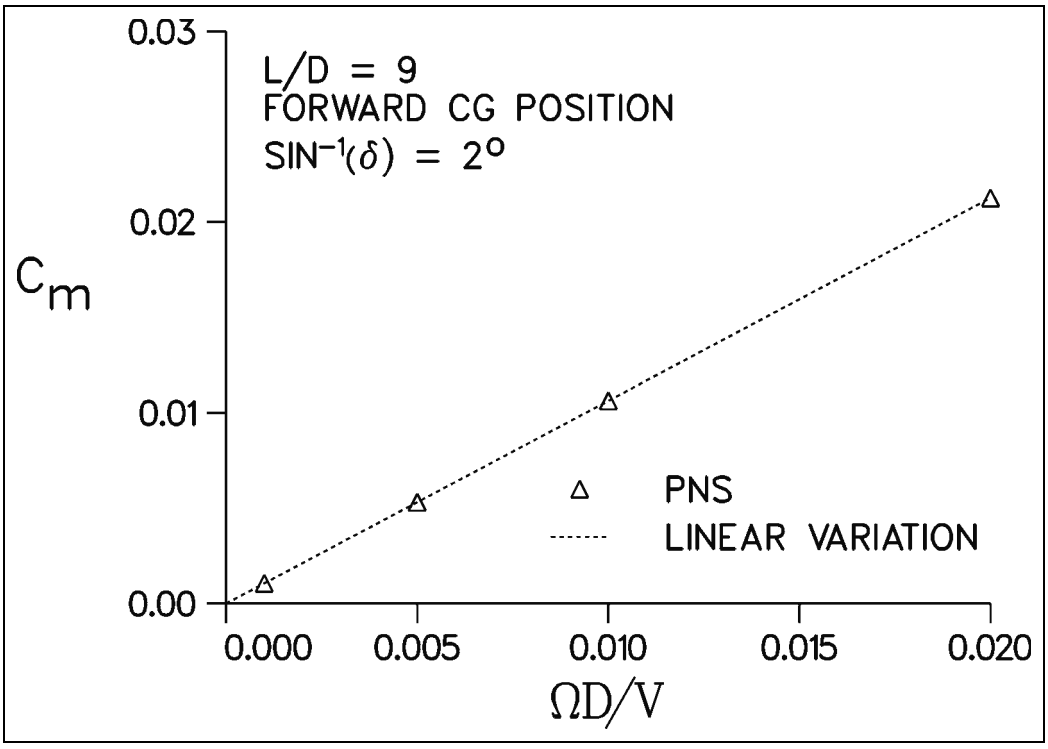


Figure 8. Variation of aerodynamic moment $C_m$ with angular velocity, q = 0 helical motion, M = 2.5, ANSR, $\sin^{-1}\delta = 2°$.

For the q = 0 helical motion, the sine of the angle of attack, $\delta$, varies directly with the rotational velocity ratio, $\frac{R_o\Omega}{V}$ (see equation 8). Thus, as the rotational velocity ratio increases toward 1, the angle of attack of the vehicle also increases for the q = 0 helical motion. (In the limit as $\frac{R_o\Omega}{V} = 1$, for q = 0 helical motion, the CG performs a circular looping motion with the body at 90° angle of attack.) The desire here is to define the limits where the forces and moments are expected to vary linearly with $\delta$ or $\frac{R_o\Omega}{V}$. Computations of q = 0 helical motion were performed with the angular rate held fixed ($\frac{\Omega D}{V} = 0.01$), while the helix radius was varied to produce the desired angle of attack. The aerodynamic moment $C_m$, shown in figure 9, shows a

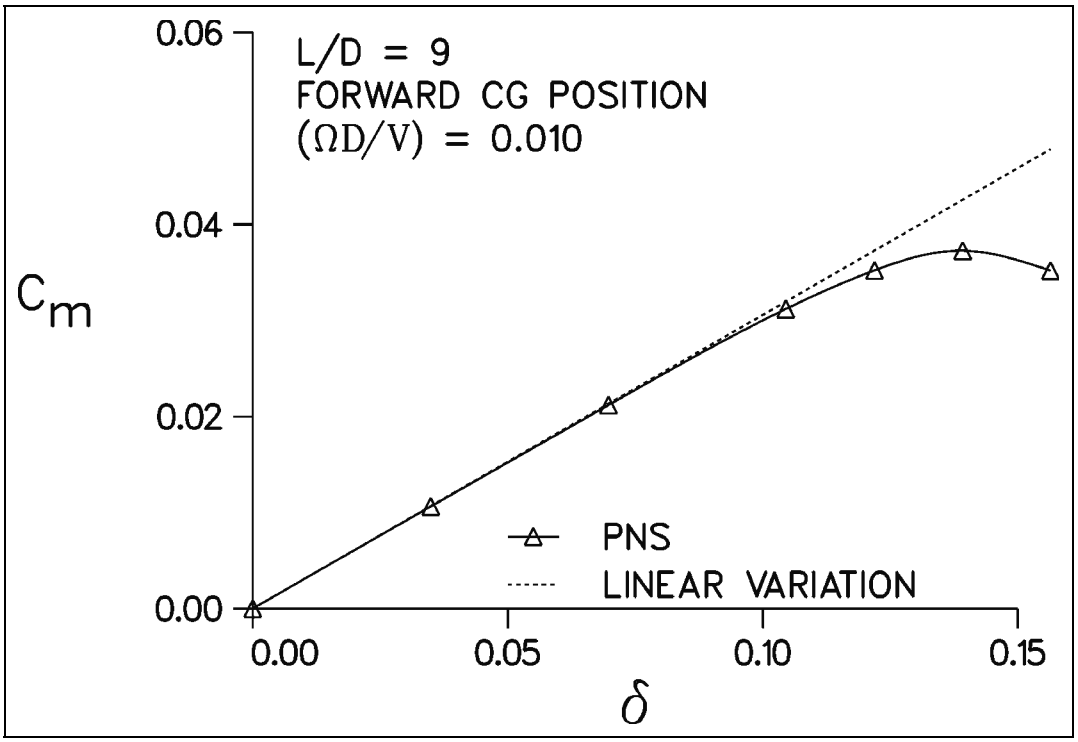


Figure 9. Variation of aerodynamic moment $C_m$ with sine of the angle of attack, q = 0 helical motion, M = 2.5, ANSR, $\frac{\Omega D}{V}$.

linear variation with $\delta$ up to angles of attack of ~7°. This behavior is similar to that observed for coning motion (*5*).

For the $\dot{\alpha} = 0$ helical motion, the effect of angular rate was examined for rotational velocity ratio, $\frac{\Omega R_o}{V} = \sin\beta = 0.0349$. Again, as the angular velocity was increased, the radius $R_o$ was decreased so that the product $R_o\Omega$ (and $\sin\beta$ ) was constant. The variation of the aerodynamic moment $C_m$ with angular velocity, shown in figure 10, is seen to be linear across the range of angular velocities of interest here.

The effect of the rotational velocity ratio $\frac{\Omega R_o}{V} = \sin\beta$ on the forces and moments for the $\dot{\alpha} = 0$ helical motion was also examined, and results are shown in figure 11. These predictions were made for a constant angular velocity, ($\frac{\Omega D}{V} = 0.01$). The aerodynamic moment $C_m$ is seen to be linear with rotational velocity ratios from 0 to 1. At first glance, a nonlinear variation might be expected since nonlinear variations with $\delta$ were seen for the q = 0 helical motion. It is noted

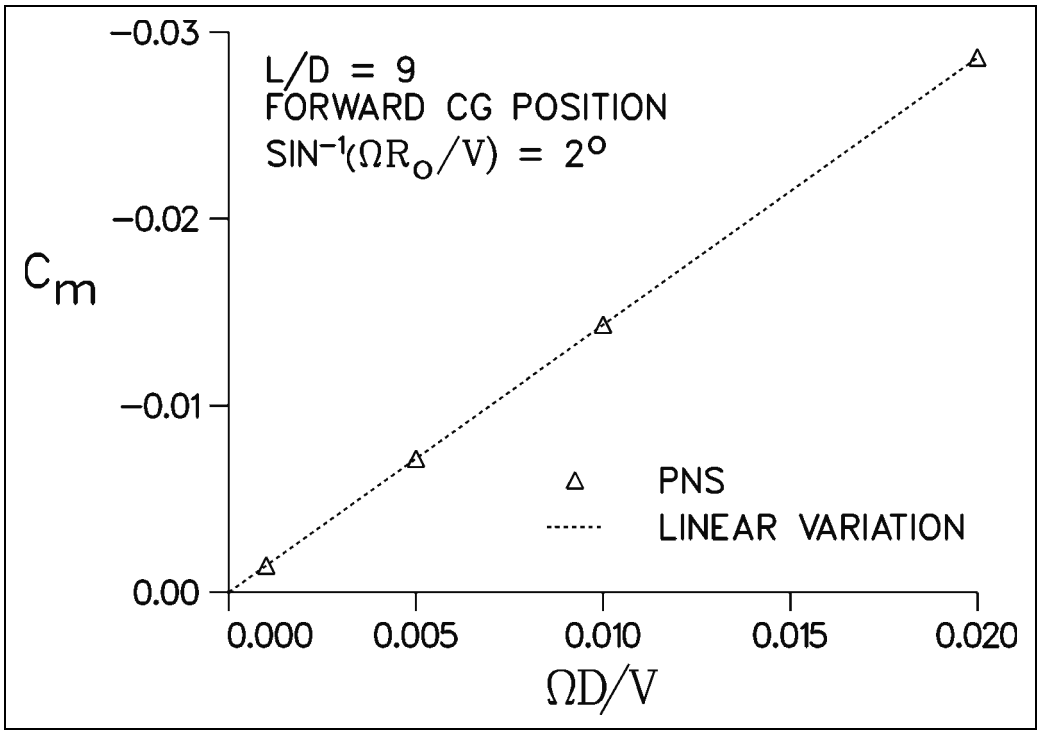


Figure 10. Variation of aerodynamic moment $C_m$ with angular velocity, $\dot{\alpha} = 0$ helical motion, M = 2.5, ANSR, $\beta = 2°$.

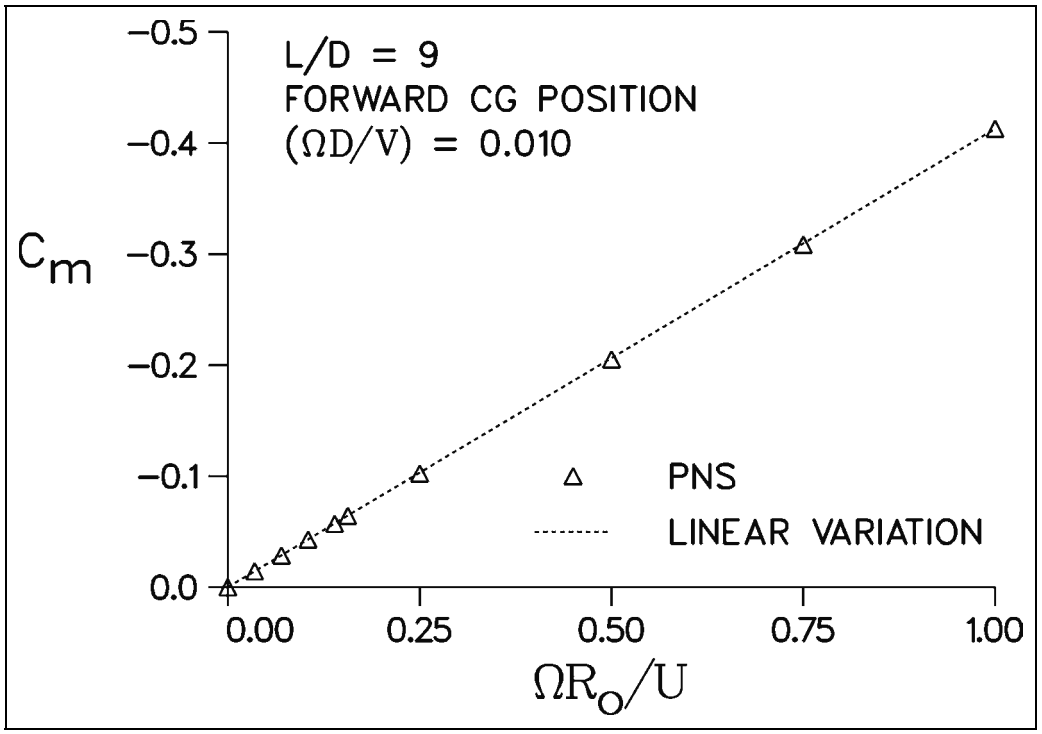


Figure 11. Variation of aerodynamic moment $C_m$ with rotational velocity ratio, $\dot{\alpha} = 0$ helical motion, M = 2.5, ANSR, $\frac{\Omega D}{V} = 0.010$.

that the parameter $\frac{\Omega R_o}{V} = \sin\beta$ is not associated with the angle of attack for this motion because the $\dot{\alpha} = 0$ helical motion is performed at 0° angle of attack. The parameter, $\sin\beta$, is simply the rotational velocity ratio which for the $\dot{\alpha} = 0$ helical motion reflects the aspect ratio of the helix. The limiting case of a rotational velocity ratio of 1 corresponds to a circular looping motion discussed previously.

Using these results as a guide, predictions of the pitch-damping coefficients were made for each of the three body lengths and three CGs at Mach 1.8 and 2.5. Predictions were made at an angular velocity of $\frac{\Omega D}{V} = 0.01$ and a rotational velocity ratio, $\frac{\Omega R_o}{V} = 0.0349$, where the linear aerodynamic theory has been shown to be valid.

Figures 12–14 show predictions of the pitch-damping moment coefficients, $C_{m_q}$ and $C_{m_{\dot{\alpha}}}$, as a function of the CG position for the L/D = 5, 7, and 9 bodies at Mach 2.5. Predictions obtained using the PNS computational approach are shown, along with results obtained with slender body theory. Both PNS and slender body predictions show that the pitch-damping coefficient $C_{m_q}$ is larger than $C_{m_{\dot{\alpha}}}$ for all the CG positions examined. The PNS prediction of the damping coefficient, $C_{m_{\dot{\alpha}}}$, is nearly zero at the rearward CG for each of the body lengths. The trends shown by the slender body results are similar to the PNS results, although the slender body predictions are generally lower in magnitude. The PNS predictions of the variation of $C_{m_q}$ with CG position shown in figures 12–14 agree with the theoretical variation (equation 24) to within 0.25% across the range of CG positions examined. The PNS predictions of the variation of $C_{m_{\dot{\alpha}}}$ are essentially identical to the theoretical variation (equation 23) because the governing equations, boundary conditions, and flow field are independent of the axial CG location.

Figures 15–17 show similar predictions of the pitch-damping force coefficients, $C_{N_q}$ and $C_{N_{\dot{\alpha}}}$, as a function of CG position for the L/D = 5, 7, and 9 bodies at Mach 2.5. The PNS predictions of the pitch-damping force coefficients show a similar trend to the predictions made with slender body theory, though the slender body theory results are larger in magnitude. The agreement does seem to improve slightly as the body length increases.

Because ballistic bodies traverse a nearly rectilinear path, it is impossible to extract the individual components of the damping coefficients from the experimental data. Thus, no comparison of the predicted individual coefficients could be made with experimental data. However, the individual coefficients can be summed to produce the pitch-damping coefficient sum, and the results compared with the coning motion results and with experiment. Figures 18–20 show comparisons of the pitch-damping coefficient sum (obtained by summing the individual coefficients) with experimental data and slender body theory results. The results

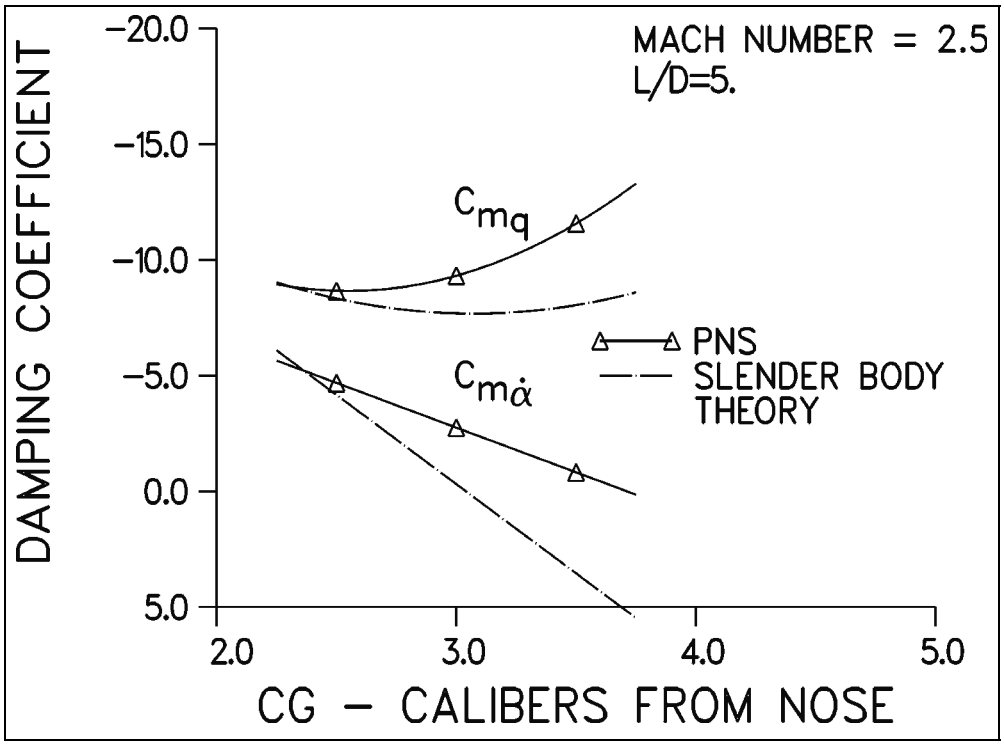


Figure 12. Variation of damping moment coefficients with CG location, M = 2.5, ANSR, L/D = 5.

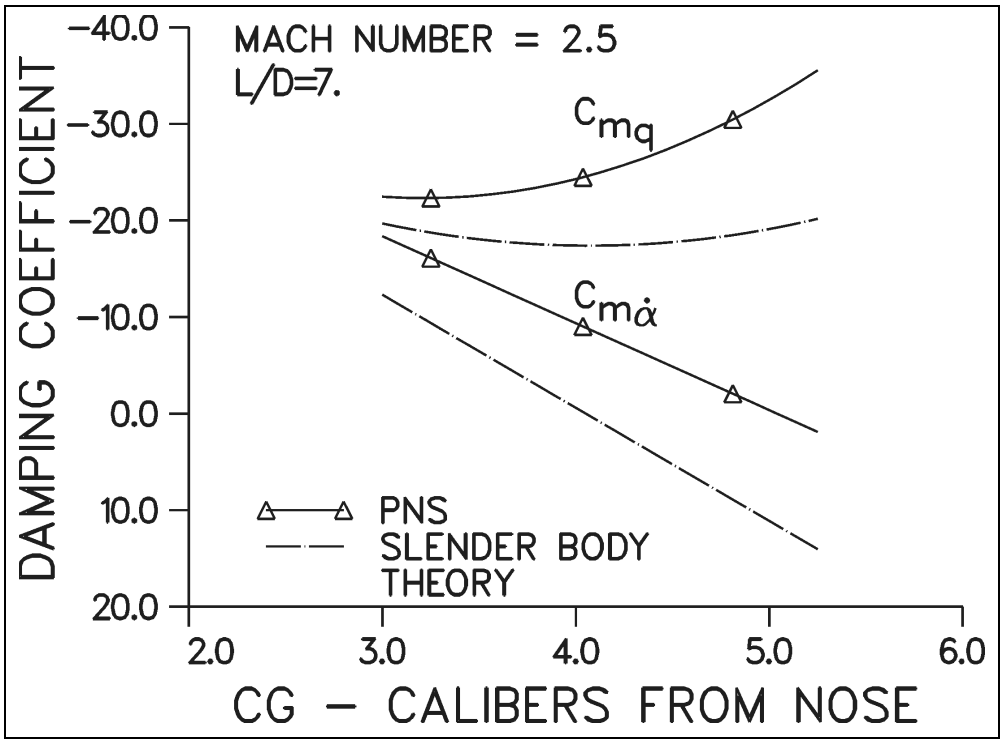


Figure 13. Variation of damping moment coefficients with CG location, M = 2.5, ANSR, L/D = 7.

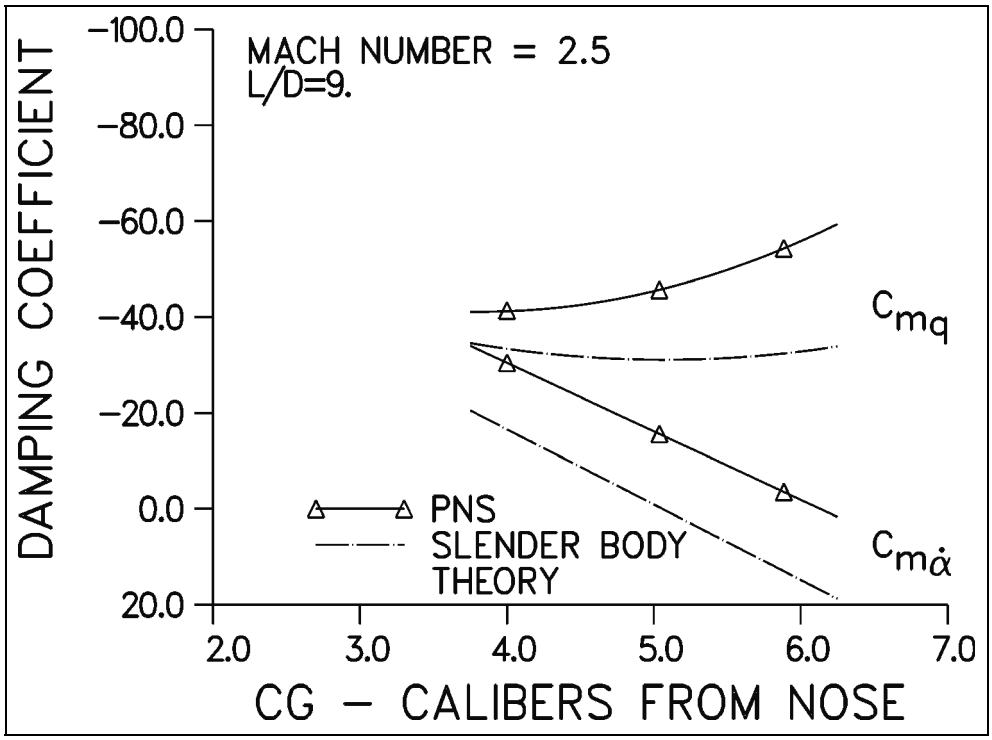


Figure 14. Variation of damping moment coefficients with CG location, M = 2.5, ANSR, L/D = 9.

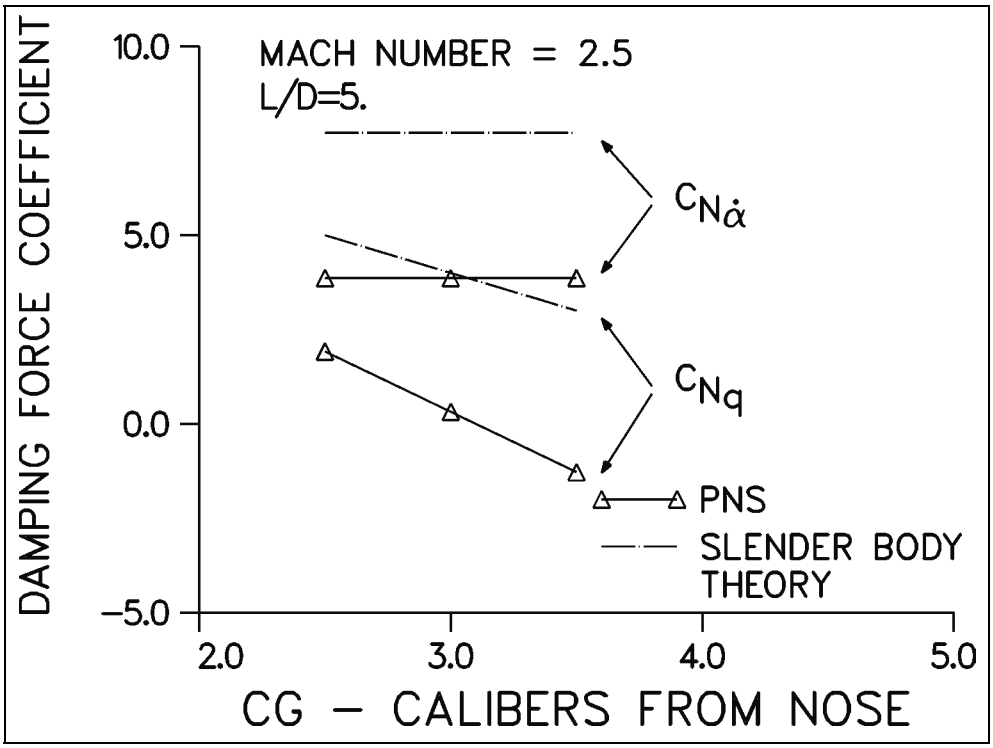


Figure 15. Variation of damping force coefficients with CG location, M = 2.5, ANSR, L/D = 5.

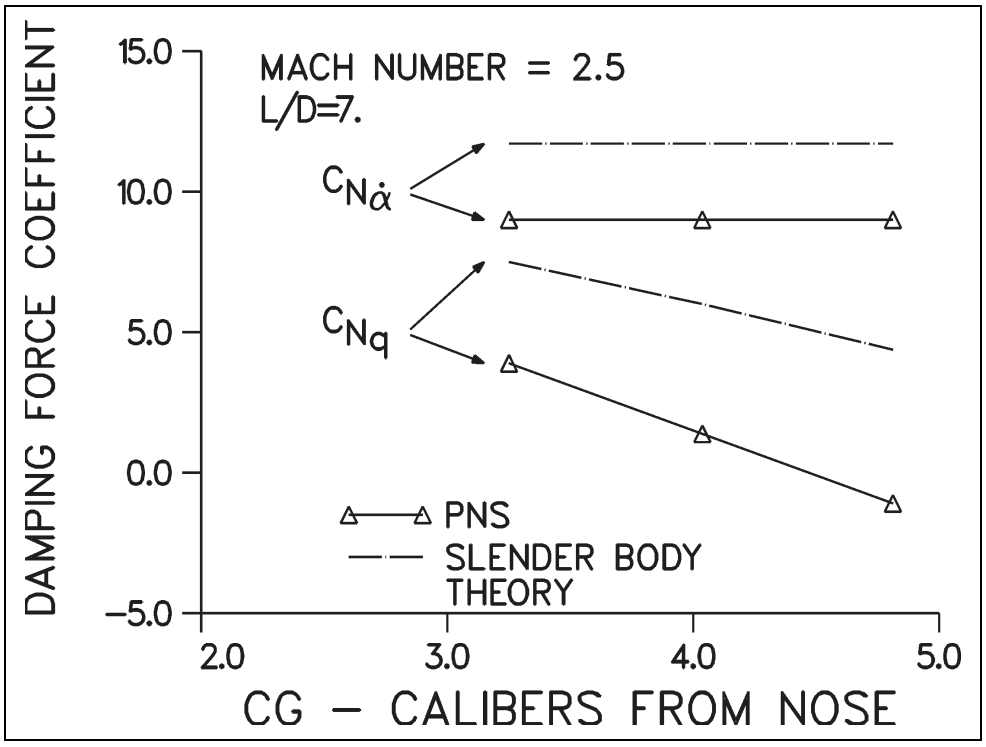


Figure 16. Variation of damping force coefficients with CG location, M = 2.5, ANSR, L/D = 7.

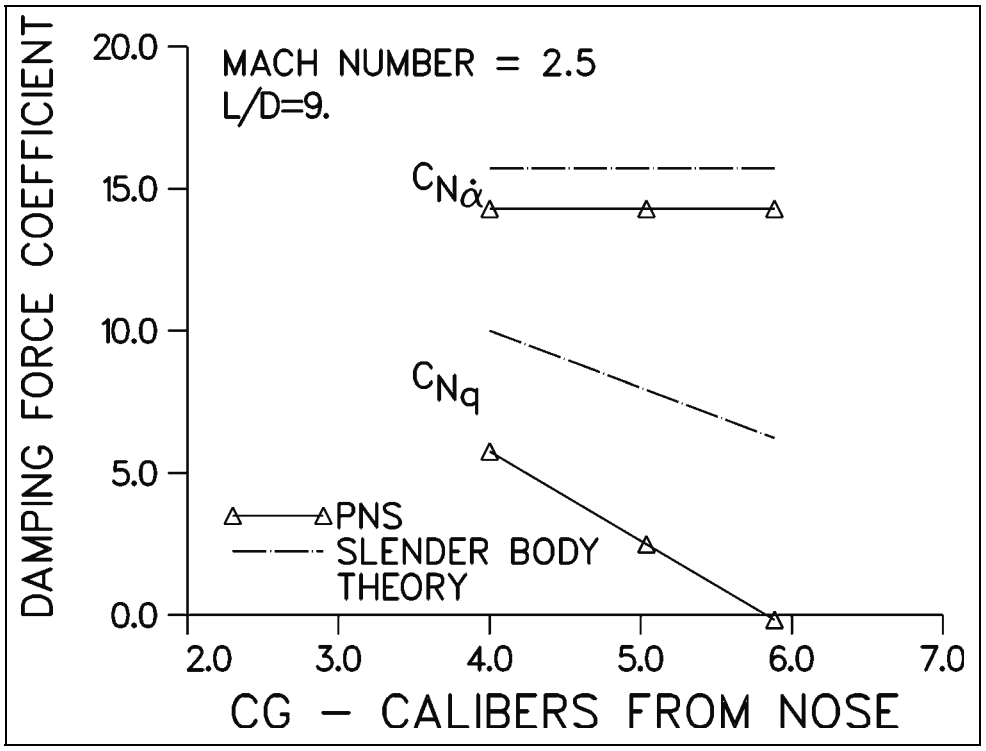


Figure 17. Variation of damping force coefficients with CG location, M = 2.5, ANSR, L/D = 9.

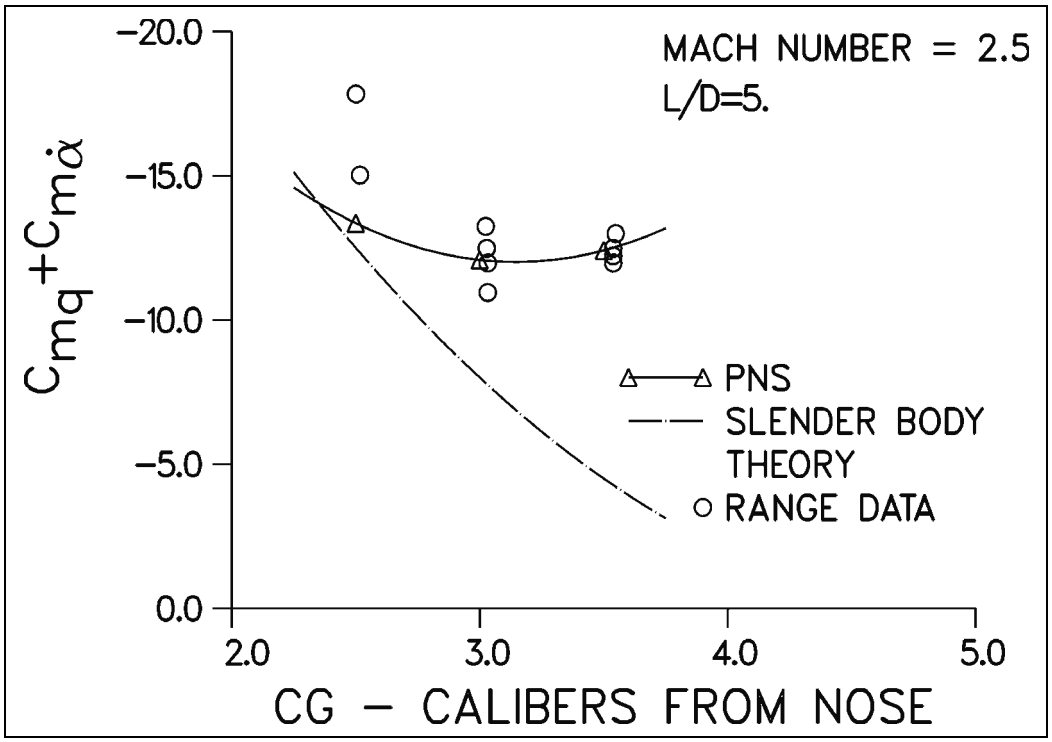


Figure 18. Variation of damping moment coefficient sum with CG location, M = 2.5, ANSR, L/D = 5.

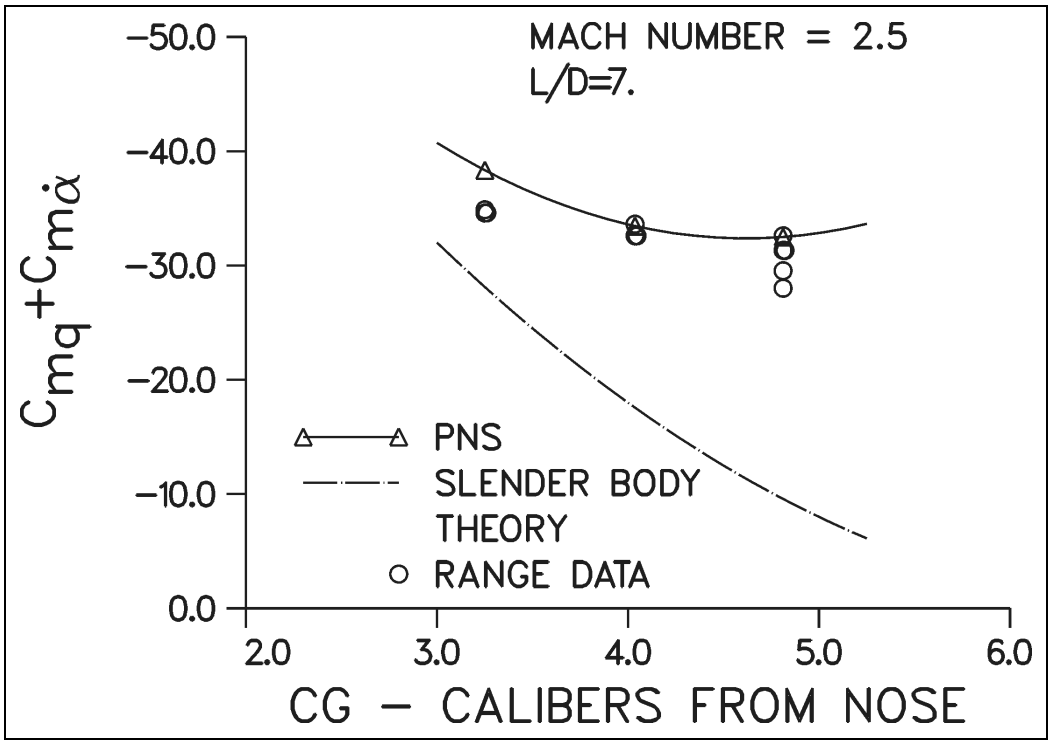


Figure 19. Variation of damping moment coefficient sum with CG location, M = 2.5, ANSR, L/D = 7.

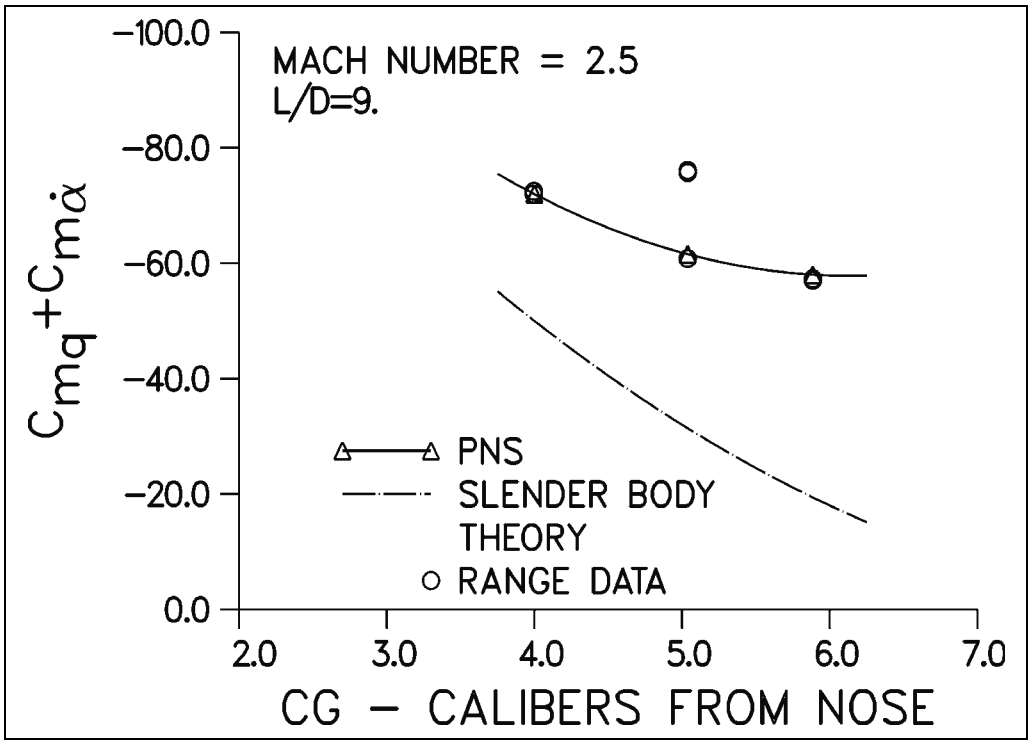


Figure 20. Variation of damping moment coefficient sum with CG location, M = 2.5, ANSR, L/D = 9.

obtained by summing the predicted coefficients, $C_{m_q}$ and $C_{m_{\dot{\alpha}}}$, are within 1.0% or less of the pitch-damping moment coefficient sum predicted using coning motion.

To provide additional validation of the current approach, the predictions were also compared with the nonlinear unsteady potential equation results obtained by Devan (*19*) for the L/D = 5 ANSR configuration. The variation in the two damping coefficients with Mach number is shown in figure 21. In general, the results show modest variations in the predicted coefficients across the Mach number range except for the slender body predictions which are independent of Mach number. The nonlinear potential solution of Devan shows good agreement with the PNS predictions with a similar variation with Mach number predicted. (It is noted that Devan did not explicitly determine the damping coefficient $C_{m_q}$, but instead computed $C_{m_{\dot{\alpha}}}$ and $(C_{m_q} + C_{m_{\dot{\alpha}}})$ from which $C_{m_q}$ can be obtained.) The approach of Devan overpredicts the two damping coefficients by 7% for $C_{m_q}$ and ~25% for $C_{m_{\dot{\alpha}}}$, compared with the PNS results. The predicted value of $C_{m_q}$ from slender body theory differs by as much as 25% with the PNS predictions. The slender body theory predicts a nearly zero value for the damping coefficient $C_{m_{\dot{\alpha}}}$, while the PNS predictions show this coefficient is ~ 25%–40% of the value of $C_{m_q}$ at the middle CG location.

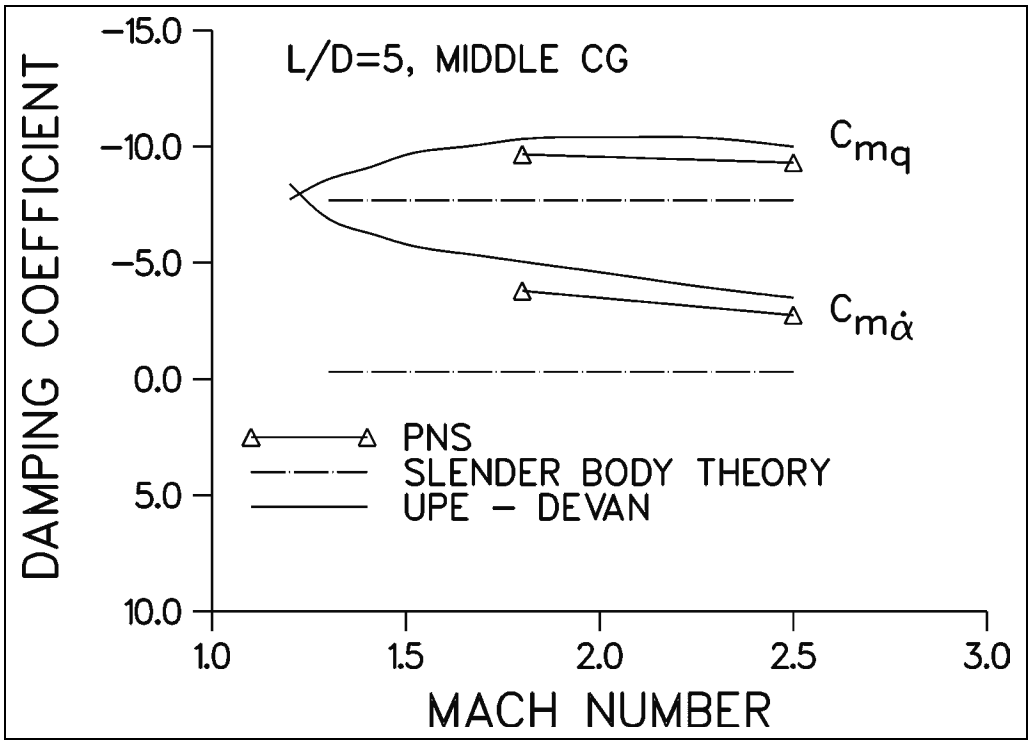


Figure 21. Variation of the pitch-damping moment coefficients with Mach number, ANSR, L/D = 5, middle CG location.

A comparison of the Mach number variation of the pitch-damping coefficient sum for the various approaches with aerodynamic range data is shown in figure 22. Compared with the slender body theory and the nonlinear unsteady potential equation results of Devan, the PNS results show the best agreement with the experimental data. The approach of Devan shows generally a similar variation with Mach number as the PNS approach and the experimental data, but appears to show a slight overprediction (~10%) across the Mach number range. This overprediction is consistent with the overprediction seen previously for the individual coefficients. The slender body theory results, which exhibit no dependence on Mach number, consistently underpredicts the pitch-damping sum by >30%.

The distribution of the pitch-damping force and moment coefficients over the ANSR L/D = 5 body is shown in figures 23 and 24. The force coefficient $C_{N_{\dot{\alpha}}}$ is positive along the body length with most of the force being generated at the aft end of the body. As a result, the moment coefficient $C_{m_{\dot{\alpha}}}$ also shows its largest contributions from the aft portion of the body. On the other hand, for the force coefficient, $C_{N_q}$, both the nose and cylindrical afterbody produce contributions to the force coefficient which are similar in magnitude but opposite in sign. This essentially imposes a couple on the body whose magnitude is reflected in the moment coefficient, $C_{m_q}$.

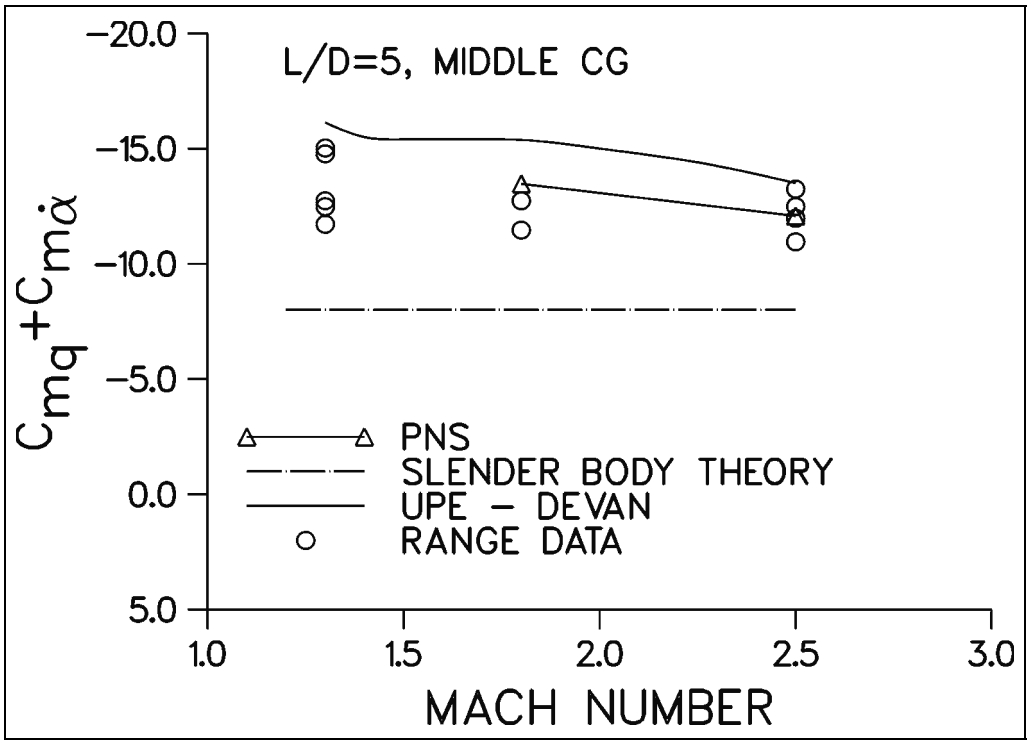


Figure 22. Variation of the pitch-damping moment coefficient sum with Mach number, ANSR, L/D = 5, middle CG location.

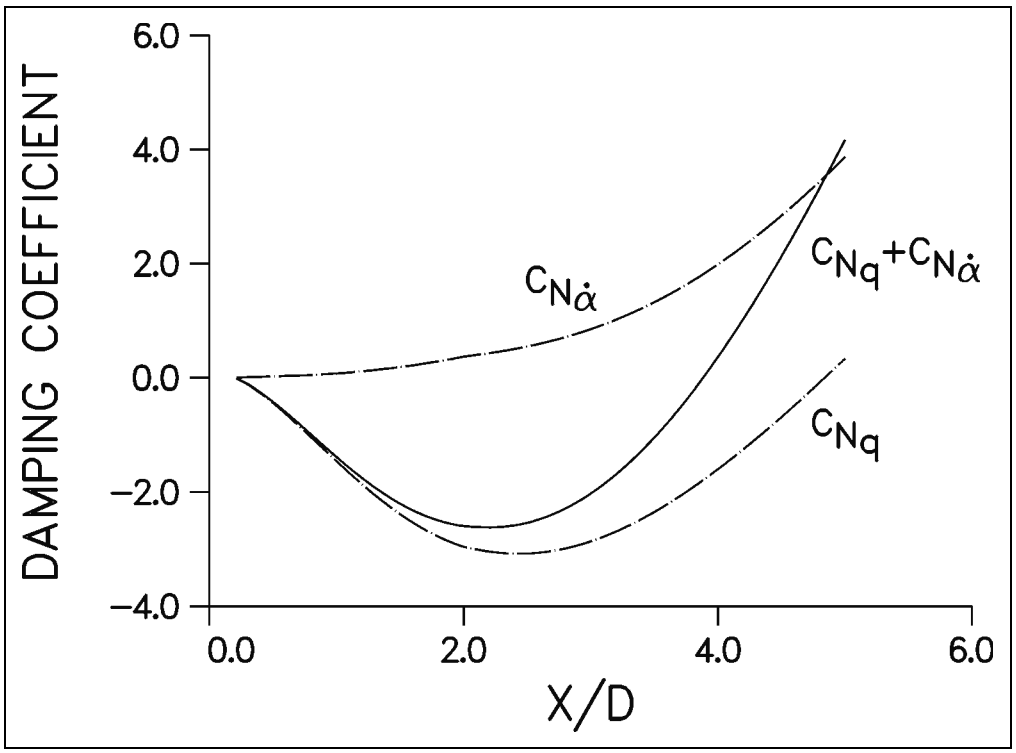


Figure 23. Development of pitch-damping force coefficients over ANSR body, M = 2.5, L/D = 5, middle CG position.

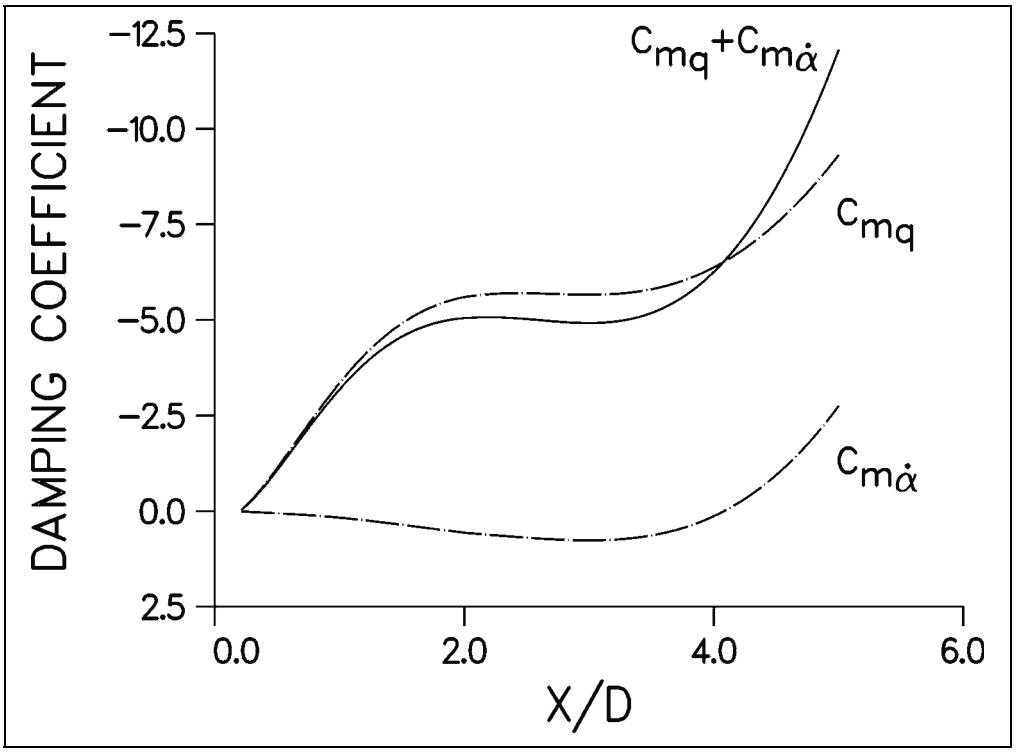


Figure 24. Development of pitch-damping moment coefficients over ANSR body, M = 2.5, L/D = 5, middle CG position.

## 5. Conclusion

A method for determining the individual force and moment coefficients that comprise the pitch-damping force and moment coefficient sum has been presented, along with sample results for a family of axisymmetric projectile geometries. The sum of the two individual coefficients is identical to previous predictions of the pitch-damping coefficient sums obtained using coning motion and is in excellent agreement with experimental data. Additional validation of the approach is obtained through comparisons with prior results from numerical solutions of the nonlinear unsteady potential equation. The individual coefficients show qualitative agreement with results obtained using the more approximate slender body theory. The method provides an efficient means of determining the individual coefficients which may be quite difficult to obtain using experimental means.

## 6. References


1. Schiff, L. B. Nonlinear Aerodynamics of Bodies in Coning Motion. *AIAA Journal* **1972**, *10* (11), 1517–1522.

2. Agarwal, R.; Rakich, J. V. Computation of Supersonic Laminar Viscous Flow Past a Pointed Cone at Angle of Attack in Spinning and Coning Motion. *AIAA Paper*, July 1978; 78–1211.

3. Lin, T. C. A Numerical Study of the Aerodynamics of a Reentry Vehicle in Steady Coning Motion. *AIAA Paper*, August 1978; 78–1358.

4. Weinacht, P.; Sturek, W. B. Navier-Stokes Predictions of Pitch-Damping for Finned Projectiles Using Steady Coning Motion. *Proceedings of the AIAA 8th Applied Aerodynamics Conference*, AIAA, Washington, DC, August 1990; AIAA Paper 90-3088, 632–642.

5. Weinacht, P.; Sturek, W. B.; Schiff, L. B. Navier-Stokes Predictions of Pitch-Damping for Axisymmetric Shell Using Steady Coning Motion. *Proceedings of the 1991 Atmospheric Flight Mechanics Conference*, AIAA, Washington, DC, August 1991; AIAA Paper 91-2855, 89–100.

6. Weinacht, P.; Sturek, W. B.; Schiff, L. B. Navier-Stokes Predictions of Pitch-Damping for Axisymmetric Shell Using Steady Coning Motion. *Journal of Spacecraft and Rockets* **1997**, *34* (6), 753–761.

7. Weinacht, P. Navier-Stokes Predictions of Pitch-Damping for a Family of Flared Projectiles. *Proceedings of the 9th Applied Aerodynamics Conference*, AIAA, Washington, DC, September 1991; AIAA Paper 91-3339, Vol. 2, 1025–1034.

8. Weinacht, P. Navier-Stokes Predictions of the Individual Components of the Pitch-Damping Coefficient Sum. *Proceedings of the 1995 Atmospheric Flight Mechanics Conference*, AIAA, Washington, DC, August 1995; AIAA Paper 95-3458, 291–301.

9. Weinacht, P. Navier-Stokes Predictions of the Individual Components of the Pitch-Damping Coefficient Sum. *Journal of Spacecraft and Rockets* **1998**, *35* (5), 598–605.

10. Weinacht, P. Prediction of Pitch-Damping Aerodynamic Derivatives Using Navier-Stokes Computational Techniques. Ph.D. Thesis, University of Delaware, Newark, DE, 1996.

11. Qin, N.; Ludlow, D. K.; Shaw, S. T.; Edwards, J. A.; Dupuis, A. Calculation of Pitch Damping Coefficients for Projectiles. *AIAA Paper 97-0405*, January 1997.

12. Murphy, C. H. *Free Flight Motion of Symmetric Missiles*; BRL-TR-1216; U.S. Army Ballistic Research Laboratory: Aberdeen Proving Ground, MD, 1963.

13. Baldwin, B. S.; Lomax, H. Thin Layer Approximation and Algebraic Model for Separated Turbulent Flows. *AIAA Paper 78-257*, January 1978.

14. Schiff, L. B.; Steger, J. L. Numerical Simulation of Steady Supersonic Viscous Flow. *AIAA Journal* **1980**, *18* (12), 1421–1430.

15. Beam, R.; Warming, R. F. An Implicit Factored Scheme for the Compressible Navier-Stokes Equations. *AIAA Journal* **1978**, *16* (4), 393–402.

16. Rai, M. M.; Chaussee, D. S. New Implicit Boundary Procedure: Theory and Applications. *AIAA Paper 83-0123*, January 1983.

17. Sturek, W. B.; Schiff, L. B. Computations of the Magnus Effect for Slender Bodies in Supersonic Flight. *Proceedings of the AIAA Atmospheric Flight Mechanics Conference*, AIAA, New York, August 1980; AIAA Paper 80-1586-CP, 260–280.

18. Murphy, C. H.; Schmidt, L. E. *The Effect of Length on the Aerodynamics Characteristics of Bodies of Revolution in Supersonic Flight*; BRL-TR-876; U.S. Army Ballistic Research Laboratory: Aberdeen Proving Ground, MD, 1953.

19. Devan, L. *Nonaxisymmetric Body, Supersonic, Inviscid Dynamic Derivative Predictions*; NSWC TR 89-99; U.S. Naval Surface Warfare Center: Dahlgren, VA, 1989.

INTENTIONALLY LEFT BLANK.

## List of Abbreviations and Symbols

| | |
|---|---|
| $a_\infty$ | Freestream speed of sound |
| $C_m$ | Pitching moment coefficient, $\frac{\overline{M}}{\frac{1}{2}\rho V^2 S_{ref} D}$ |
| $C_{m_\alpha}$ | Pitching moment coefficient slope with respect to angle of attack, $\frac{\partial C_m}{\partial \alpha}$ |
| $C_{m_{\dot{\alpha}}}$ | Pitch-damping moment coefficient slope, $\frac{\partial C_m}{\partial\left(\frac{\dot{\alpha} D}{V}\right)}$ |
| $C_{m_q}$ | Pitch-damping moment coefficient slope, $\frac{\partial C_m}{\partial\left(\frac{q D}{V}\right)}$ |
| $C_{m_q} + C_{m_{\dot{\alpha}}}$ | Pitch-damping moment coefficient |
| $C_n$ | Side moment coefficient |
| $C_{n_{p\alpha}}$ | Magnus moment coefficient, $\frac{\partial^2 C_n}{\partial\left(\frac{p D}{V}\right)\partial \alpha}$ |
| $C_N$ | Normal force coefficient, $\frac{\overline{F}}{\frac{1}{2}\rho V^2 S_{ref}}$ |
| $C_{N_\alpha}$ | Normal force coefficient slope with respect to angle of attack, $\frac{\partial C_N}{\partial \alpha}$ |
| $C_{N_{\dot{\alpha}}}$ | Pitch-damping force coefficient slope, $\frac{\partial C_N}{\partial\left(\frac{\dot{\alpha} D}{V}\right)}$ |
| $C_{N_q}$ | Pitch-damping force slope, $\frac{\partial C_N}{\partial\left(\frac{q D}{V}\right)}$ |
| $C_{N_q} + C_{N_{\dot{\alpha}}}$ | Pitch-damping force coefficient |

| | |
|---|---|
| $D$ | Reference diameter |
| $e$ | Total energy per unit volume |
| $\hat{E}, \hat{F}, \hat{G}$ | Flux vectors in transformed coordinates |
| $f_x, f_\phi, f_r$ | Component of acceleration vector $\vec{f}$ in the $x$, $\phi$, and $r$ directions |
| $\overline{F}$ | Force |
| $\hat{H}$ | Source term in Navier-Stokes equations due rotating coordinate frame |
| $\hat{H}_c$ | Inviscid source term due to cylindrical coordinate formulation |
| $J$ | Jacobian |
| $\ell$ | Characteristic length, typically D |
| $L$ | Body length |
| $\overline{M}$ | Moment |
| $M$ | Freestream Mach number |
| $p$ | Pressure, as used in Navier-Stokes equations |
| $p$ | Spin rate, as used in roll equations |
| $q, r$ | Transverse angular rates of body along $y$ and $z$ directions |
| $r$ | Radial coordinate as used in Navier-Stokes equations |
| $\vec{R}$ | Displacement vector between the axis of rotation and location in flow field |
| $R_o$ | Helix radius or radius of circular arc for looping motion |
| $Re$ | Reynolds number, $a_\infty \rho_\infty D / \mu_\infty$ |
| $s$ | Distance downrange |
| $s_{cg}$ | Center of gravity shift in calibers |
| $S_{ref}$ | Reference area, $S_{ref} = \frac{\pi D^2}{4}$ |
| $\hat{S}$ | Viscous flux vector |
| $\hat{S}_c$ | Additional viscous terms due to cylindrical coordinate formulation |
| $t$ | Time |

| | |
|---|---|
| $u, v, w$ | Velocity components in the three directions |
| U | Vehicle velocity alone helix axis |
| V | Magnitude of freestream velocity |
| $\vec{V}_\infty$ | Freestream velocity vector |
| $x, y, z$ | Axial, horizontal, and vertical coordinates |
| $x_e, y_e, z_e$ | Three-dimensional coordinate in earth-fixed system |
| $x_{cg}$ | Axial location of center of gravity |
| $y^+$ | Nondimensional boundary layer coordinate |

**Greek Symbols**

| | |
|---|---|
| $\alpha$ | Angle of attack |
| $\dot{\alpha}$ | Angular rate associated with angle of attack |
| $\beta$ | Angle between helix axis and longitudinal body axis for $\dot{\alpha} = 0$ helical motion |
| $\gamma$ | Ratio of specific heats, in Navier-Stokes equations |
| $\gamma$ | Cosine of total angle of attack, as used in the aerodynamic force and moment equations |
| $\delta$ | Sine of the total angle of attack |
| $\theta$ | Angular orientation of body relative to inertial frame for looping motion |
| $\mu, \mu_t$ | Laminar and turbulent viscosity |
| $\tilde{\mu}$ | Complex transverse angular velocity |
| $\xi, \eta, \zeta$ | Transformed coordinates in the Navier-Stokes equations |
| $\tilde{\xi}$ | Complex angle of attack |
| $\rho$ | Density |
| $\phi$ | Circumferential coordinate, measured from the vertical axis |
| $\Omega$ | Angular rate associated with looping and helical motions |

**Superscripts**

| | |
|---|---|
| $\dot{(\,)}$ | Rate of change with respect to time |
| $(\,)'$ | Rate of change with respect to space |
| $\tilde{(\,)}$ | Referenced to nonrolling coordinate frame |

**Subscripts**

| | |
|---|---|
| $\infty$ | Quantity evaluated at freestream conditions |

| NO. OF COPIES | ORGANIZATION |
|---|---|
| 1 (PDF Only) | DEFENSE TECHNICAL INFORMATION CENTER<br>DTIC OCA<br>8725 JOHN J KINGMAN RD<br>STE 0944<br>FT BELVOIR VA 22060-6218 |
| 1 | COMMANDING GENERAL<br>US ARMY MATERIEL CMD<br>AMCRDA TF<br>5001 EISENHOWER AVE<br>ALEXANDRIA VA 22333-0001 |
| 1 | INST FOR ADVNCD TCHNLGY<br>THE UNIV OF TEXAS<br>AT AUSTIN<br>3925 W BRAKER LN STE 400<br>AUSTIN TX 78759-5316 |
| 1 | US MILITARY ACADEMY<br>MATH SCI CTR EXCELLENCE<br>MADN MATH<br>THAYER HALL<br>WEST POINT NY 10996-1786 |
| 1 | DIRECTOR<br>US ARMY RESEARCH LAB<br>AMSRD ARL D<br>DR D SMITH<br>2800 POWDER MILL RD<br>ADELPHI MD 20783-1197 |
| 1 | DIRECTOR<br>US ARMY RESEARCH LAB<br>AMSRD ARL CS IS R<br>2800 POWDER MILL RD<br>ADELPHI MD 20783-1197 |
| 3 | DIRECTOR<br>US ARMY RESEARCH LAB<br>AMSRD ARL CI OK TL<br>2800 POWDER MILL RD<br>ADELPHI MD 20783-1197 |
| 3 | DIRECTOR<br>US ARMY RESEARCH LAB<br>AMSRD ARL CS IS T<br>2800 POWDER MILL RD<br>ADELPHI MD 20783-1197 |

| NO. OF COPIES | ORGANIZATION |
|---|---|
| | ABERDEEN PROVING GROUND |
| 1 | DIR USARL<br>AMSRD ARL CI OK TP (BLDG 4600) |

NO. OF
COPIES ORGANIZATION

1 ARROW TECH ASSOCIATES
W HATHAWAY
1233 SHELBURNE RD
D 8
BURLINGTON VT 05403

1 OREGON STATE UNIVERSITY
DEPT OF MECH ENGINEERING
M COSTELLO
CORVALLIS OR 97331

1 ATK
R DOHRN
MN07 LW54
4700 NATHAN LN N
PLYMOUTH MN 55442

1 AEROPREDICTION INC
F MOORE
9449 GROVER DR
SUITE 201
KING GEORGE VA 22485

1 COMMANDER ARDEC
AMSTR AR FSF X
W TOLEDO
BLDG 95 SOUTH
PICATINNY ARSENAL NJ 07806-5000

ABERDEEN PROVING GROUND

21 DIR USARL
AMSRD ARL WM B
A HORST
AMSRD ARL WM BA
D LYON
AMSRD ARL WM BC
M BUNDY
G COOPER
J DESPIRITO
J GARNER
B GUIDOS
K HEAVEY
J NEWILL
P PLOSTINS
J SAHU
S SILTON
D WEBB
P WEINACHT (5 CPS)
A ZIELINSKI
AMSRD ARL WM BD
B FORCH
AMSRD ARL WM BF
S WILKERSON